WIRELESS RADIO FREQUENCY SENSORS FOR STRUCTURAL HEALTH MONITORING

A THESIS
SUBMITTED TO THE DEPARTMENT OF ELECTRICAL AND ELECTRONICS ENGINEERING
AND THE GRADUATE SCHOOL OF ENGINEERING AND SCIENCES
OF BILKENT UNIVERSITY
IN PARTIAL FULLFILMENT OF THE REQUIREMENTS
FOR THE DEGREE OF
MASTER OF SCIENCE

By
Hatice Ertuğrul
August 2011

I certify that I have read this thesis and that in my opinion it is fully adequate, in scope and in quality, as a thesis for the degree of Master of Science.

Assoc. Prof. Dr. Hilmi Volkan Demir (Co-supervisor)

I certify that I have read this thesis and that in my opinion it is fully adequate, in scope and in quality, as a thesis for the degree of Master of Science.

Assoc. Prof. Dr. Vakur B. Ertürk (Co-supervisor)

I certify that I have read this thesis and that in my opinion it is fully adequate, in scope and in quality, as a thesis for the degree of Master of Science.

Prof. Dr. Ergin Atalar

I certify that I have read this thesis and that in my opinion it is fully adequate, in scope and in quality, as a thesis for the degree of Master of Science.

Prof. Dr. Sencer Koç

Approved for the Graduate School of Engineering and Sciences:

Prof. Dr. Levent Onural
Director of Graduate School of Engineering and Sciences

ABSTRACT
WIRELESS RADIO FREQUENCY SENSORS FOR STRUCTURAL HEALTH MONITORING

Hatice Ertuğrul
M.S. in Electrical and Electronics Engineering
Supervisors: Assoc. Profs. Drs. Hilmi Volkan Demir and Vakur B. Ertürk
August 2011

Structural health monitoring (SHM) is fundamentally important in civil engineering. Sensing transient changes in strain build-up of a construction is essential for determining and assessing mechanical health of its structure. To date different types of strain sensors have been reported to monitor strain. However, it is technically challenging to design and operate a strain sensor at a reduced complexity and cost, while also achieving strain assessment in plastic deformation. In this study, to address this challenge, we propose a new class of wireless radio frequency (RF) strain sensors based on metamaterial-inspired architectures that allow for real-time SHM including the plastic deformation of steel rods. Such a capability is vitally critical especially in geographical locations where earthquakes frequently occur.

To enable telemetric strain sensing for SHM, we developed cost-effective, easy-to-make, passive RF sensors composed of comb-like split ring resonators, each with a cut between the two halves making the splits and a wire jumper on one end making the ring. By externally applying loads on standard steel rods, which are used in buildings, we demonstrated that the frequency shift in S_{11} changes with the gap width and the applied load, and that the displacement on the steel rods can be monitored telemetrically. Our results indicate that these wireless sensors hold great promise for real-time remote SHM.

Keywords: Wireless sensors, split ring resonators, structural health monitoring.

ÖZET

YAPISAL SAĞLIK İZLEMEYE UYGUN KABLOSUZ RADYO FREKANSI SENSÖRLERİ

Hatice Ertuğrul
Elektrik ve Elektronik Mühendisliği Bölümü Yüksek Lisans
Tez yöneticileri: Doç. Dr. Hilmi Volkan Demir ve Vakur B. Ertürk
Ağustos 2011

Yapısal sağlık izleme inşaat mühendisliği için büyük önemi olan bir konudur. Herhangi bir yapının mekanik sağlık durumunu belirlemek için yapıdaki küçük gerilim değişikliklerini gerçek zamanlı olarak gözlemleyebilmek gerekir. Bugüne kadar çeşitli gerilim sensörü türleri tasarlanmış ve yapılardaki gerilimi gözlemek için kullanılmıştır. Fakat basit tasarımı olan, düşük maliyetli ama aynı zamanda plastik deformasyon esnasında hassas ölçüm yapabilen bir gerilim sensörü tasarlamak ve çalışmasını sağlamak teknik olarak zor bir iştir. Biz bu aşamada bütün bu zorluklara bir çözüm getimek amacıyla gerçek zamanlı yapısal sağlık izlemede plastik deformasyon esnasında da kullanılabilecek, metamalzeme mimarisine dayalı, kablosuz ve radyo frekansında çalışabilecek basit bir gerilim sensörü öneriyoruz. Bu tür bir sensörü özellikle depremlerin sık yaşandığı coğrafi bölgelerde kullanmak büyük avantajlar sağlayabilir.

Yapısal sağlık izleme için telemetrik olarak gerilim ölçmede kullanılmak üzere maliyeti düşük, yapımı kolay, pasif, radyo frekansında çalışan ve tarak benzeri yarıklı halka rezonatörlerin kesilip bir tel yardımıyla tekrar birleştirilmesinden oluşan sensör yapısı geliştirdik. Gerçek binalarda kullanılan çelik donatıya dışarıdan bir çekme kuvveti uygulanmasıyla birlikte S_{11} grafiğinde frekans kayması meydana geldiğini, bu frekans kayma miktarının sensör aralığı ve yük miktarıyla orantılı olarak değiştiğini gözlemledik ve

böylece çelik çubukta meydana gelen uzama miktarını telemetrik olarak belirledik. Sonuçlarımız geliştirdiğimiz kablosuz sensörlerin gerçek zamanlı uzaktan yapısal sağlık izleme için uygun olabileceğini göstermektedir.

Anahtar Kelimeler: Kablosuz sensörler, yarıklı halka rezonatörler, yapısal sağlık izleme.

Acknowledgements

It is my pleasure to express sincere gratitude and respect to my supervisors Assoc. Prof. Dr. Vakur B. Erturk and Assoc. Prof. Dr. Hilmi Volkan Demir for their invaluable guidance, encouragement, helpful suggestions and endless support throughout the development of this thesis. Their personal and academic virtue shaped my academic personality and changed my approach to scientific study. I am very lucky to have the opportunity to study under their tutelage.

I would like to thank to the members of my thesis committee, Prof. Dr. Ergin Atalar and Prof. Dr. Sencer Koç from METU, for reading the thesis and commenting on it.

Very special thanks to Emre Ünal from whom I learnt a lot during the experiments. His invaluable support and superior motivation during my difficult times kept me standing.

I would also like to thank to Assist. Prof. Dr. Özgür Kurç and Dr. Ramazan Özçelik for their collaboration in the experiments at Middle East Technical University Civil Engineering Department Laboratory.

I am very fortunate to have been a member of the Demir Group, where I had a chance to work together and benefit from brilliant, intelligent and excited people. I am indebted to Dr. Rohat Melik for teaching how to use CST Microwave Studio and guiding me at the very beginning of my academic study.

I appreciate Asli Ünlügedik for her great advice, endless help and continuous support. Her friendship is invaluable to me. I would like to express my special thanks to Neslihan Çiçek for her friendship.

I would like to thank my office mates, Burak Şekerlisoy, Aykut Yıldız, and Behnam Ghassemiparvin for creating a fruitful working environment. It is a great pleasure to work together with such nice and hardworking friends.

Very special thanks to Mürüvet Parlakay, for making my life easier.

There is a long list of my close friends, whether old or new, far away or nearby; to feel their existence is my life source. Thank you all.

I would like to express my endless thanks to my mother, father and brother for their love, encouragement and care. I cannot imagine finishing all my achievements without their endless moral support. I dedicate this work to my mother and brother.

The Scientific and Technological Research Council of Turkey (TÜBİTAK) is acknowledged for supporting me with the graduate scholarship of TÜBİTAK BİDEB during my thesis study.

Table of Contents

List of Figures

No table of figures entries found.

No table of figures entries found.

No table of figures entries found. List of Tables

No table of figures entries found.

No table of figures entries found.

To my mother and brother...

Chapter 1

Introduction

Among various sensors in general, wireless ones tend to be more preferable compared to wired counterparts because of their typical advantages of allowing for telemetric measurements, and being smaller in size and more cost effective [1-4]. Besides, the additional use of wires may also lead to increased weight in the case of wired sensors. For wireless sensors, passive ones offer strategic advantages over active ones. Active sensors need power supplies (e.g., a battery) to function whereas passive sensors make use of the incident energy, which is externally generated. Incorporation of such a power source into a sensor, though, substantially increases the cost, weight and size of the sensor. Furthermore, the need for a source may limit potential application areas of a strain sensor and makes it impractical for its long term usage. Therefore, passive strain sensors are typically more preferable than active sensors for continuous real-time structural health monitoring (SHM), provided that they reach sufficient sensitivity.

Accurate sensing capacity is critically important in strain sensing for SHM, which requires sensors capable of detecting small strain variations in a structure. For example, such tiny strain variations can indicate problems in the structure

that can later lead to fatal damages in the whole civil infrastructure if not detected earlier. However, the majority of available strain sensors suffer limitations and they are not necessarily optimized for SHM [5-8]. To cater these needs for SHM discussed above, we propose passive, wireless sensor architectures for real-time SHM.

This thesis will be organized as follows. In the second chapter, we will describe our wireless radio frequency sensors. Then, we will identify the operating principle of our sensor and give the definitions of stress, strain and Young modulus. Next, we will have a theoretical introduction to split ring resonator (SRR) structures. Different types of SRRs including multi split ring resonator and comb-like split ring resonator structures will be explained briefly. Later, in the fourth chapter, we will observe the simulation results of the multi SRR and comb-like SRR structures in detail. We will discuss the effects of the number of the rings in the multi SRR structure and effects of the number of the teeth in the comb-like SRR structure. We will present the design steps of the printed loop antenna and also show the simulation results of the full setup with both the antenna and comb-like SRR sensor.

In chapter 5, we first clarify the experimental procedure and error criterion. We then present displacement experiment results of a proof-of-concept study in which the experiment setup is designed for controlled precise positioning of parts of the comb sensors. Next, we show the results of the loading experiments that are conducted with the experimental apparatus for mechanical loading in scaled-down version of a building. Finally, we present the real loading experiments which are obtained by applying a load to the steel rods mimicking loading in a building. Real experiment results with a concrete piece are given in this chapter. Finally, the last chapter includes a brief summary of the results obtained during this thesis work and future steps.

Chapter 2

Wireless Radio Frequency Sensors

Wireless radio frequency sensors that we developed are cost-effective, easy-to-make, passive sensors composed of comb-like split ring resonators, each with a cut between the two halves making the splits and a wire jumper on one end making the ring as shown in Figure 2.1. Different from the previous usage of a comb-like split ring resonator structure as a sensor [9], our new approach can be seen in the sensor geometry since our structure consists of two halves. These halves are mechanically separated from each other but they are electrically connected. Therefore, our sensor does not experience a distributed deformation. Only the two halves separate as a result of the strain change in the structure on which the sensor is fixed.

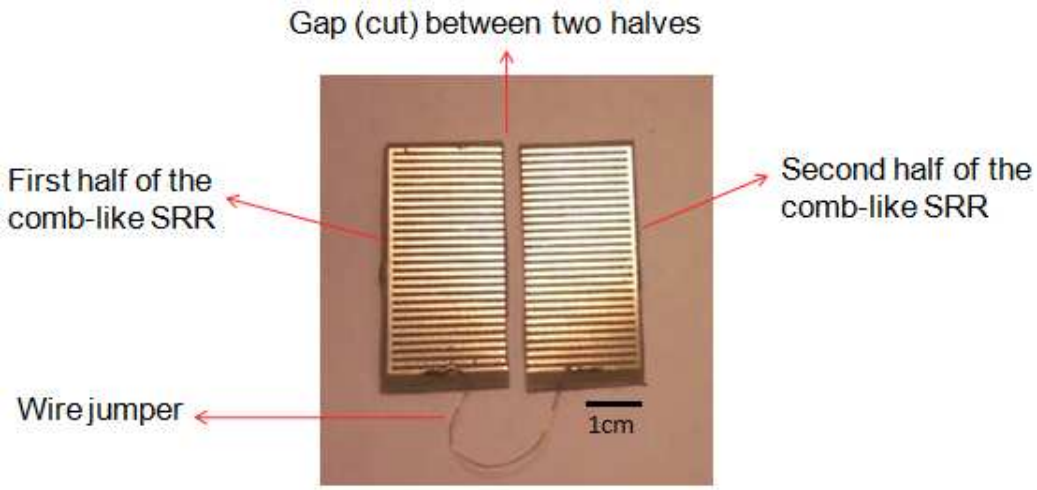

Figure 2.1 Our wireless radio frequency sensor.

To obtain our wireless radio frequency sensors, designed comb-like SRR structure has been cut into two pieces from the gap between teeth. A nearly 2 cm

long copper wire with a 0.2 mm diameter has been soldered as a jumper to these two pieces to provide an electrical connection between them. The length of the jumper should be determined carefully. The jumper should be long enough to allow mechanical separation between the two halves. However, it should not be too long because the long wire piece behaves itself as an antenna, which is not desired.

2.1 Operating Principle of Our Sensor

The working mechanism of our sensing system can be explained as follows: The proposed sensor is mounted on a part of the structure on which strain is induced. At a distance is placed a printed loop antenna, which is connected to one port of a network analyzer. Externally, an RF signal coming from our remote printed loop antenna illuminates the sensor as shown in Figure 2.2. We initially monitor the starting level of S_{11} using the antenna and assume this level as the initial strain state. Subsequently, a variation in the strain of the structure on which the sensor is fixed, slightly displacing the two cut halves of the sensor, results in a frequency shift in the S_{11} response. Examination of the frequency shift in S_{11} across a small spectral interval indicates that there is a monotonous relation between the frequency shift and the amount of load or strain variation. Resultantly, the information of strain variation can potentially be used for structural health monitoring.

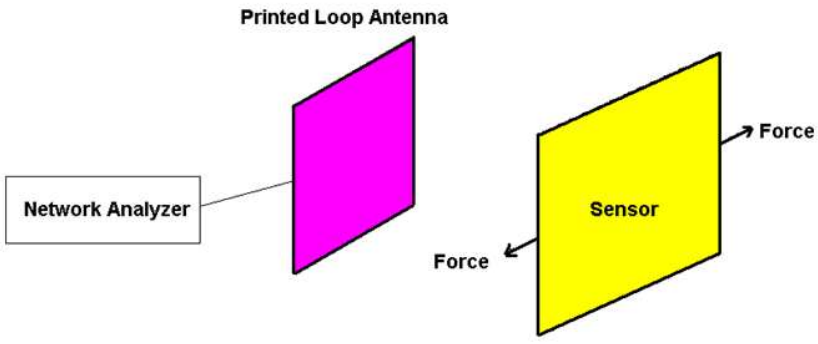

Figure 2.2 Experiment setup.

2.2 Stress, Strain and Young Modulus

It is important to clarify the definitions of stress and strain because stress, strain and elongation amount of the steel rod should be observed to evaluate the experiment results. Amount of stress in the structure can be calculated from (1):

$$\sigma = \frac{F}{A} \tag{1}$$

where σ is the stress in the structure, F is an amount of applied load and A is the cross sectional area of the structure. When the load is in N and area is in m^2, the resultant stress is in Pa.

Strain in the structure can be obtained from the strain gauges. In addition, it can be calculated from the elongation amount with the help of (2):

$$e = \frac{\Delta L}{L} \tag{2}$$

where e is the engineering strain, L is the original length of the structure and ΔL is the amount of change in the length of the structure. It is clear that the strain is a unitless quantity.

The ratio between the stress and strain is defined to be the Young modulus as shown in (3):

$$E = \frac{\sigma}{e} \tag{3}$$

where E is the Young modulus or modulus of elasticity, σ is the stress in the structure, e is the engineering strain. Young modulus is in Pa since the stress is in Pa and strain is unitless.

Chapter 3

Split Ring Resonators

Electrical and magnetic properties of the materials can be described by using two important parameters that are dielectric permittivity (ε) and magnetic permeability (μ). These two parameters can be used to understand the material response to the electric and magnetic waves. When both the real part of the dielectric permittivity and real part of the magnetic permeability are positive, electromagnetic waves can propagate in materials and so these materials are called right-handed media. Also, materials with negative permittivity and negative permeability allow the wave propagation and they are called left-handed media. On the other hand, if either the permittivity or permeability of a material is negative, electromagnetic waves cannot propagate in the material and so there occur evanescent waves. Figure 3.1 shows the right-hand and left-hand regions.

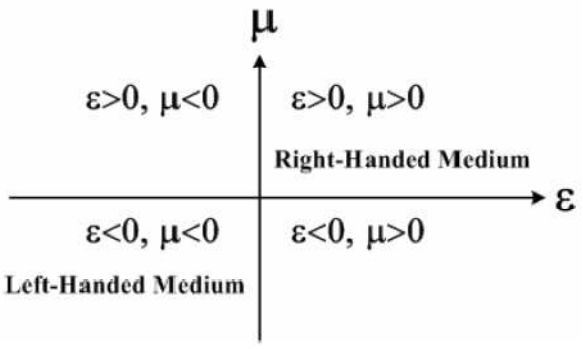

Figure 3.1 Dielectric permittivity and magnetic permeability regions.

Both the dielectric permittivity and magnetic permeability have positive values for ordinary materials in general. However, some materials including metals and periodically arranged metallic wires can have negative permittivity

for certain frequencies [10-12]. Although there are no natural materials with negative permeability, some artificially engineered materials called left-handed materials (LHM) can have both negative effective permittivity and permeability. In 1968, Veselago proposed the idea of left-handed material theoretically. It has been observed that the phase velocity of an electromagnetic wave is in the opposite direction with the group velocity in these materials. Furthermore, wave propagation and energy flow are in opposite directions in left-handed materials [13].

Periodic arrangement of thin wires can provide negative dielectric permittivity and, thus, electromagnetic wave propagation is prevented below the plasma frequency in the microwave regime [11,14,15]. Despite the presence of electric charges which provide negative permittivity, there are no magnetic charges to obtain negative permeability in the materials. Therefore, it is hard to observe negative magnetic permeability in ordinary materials. To achieve a negative permeability for frequencies close to the magnetic resonance frequency, artificial structures called split ring resonators (SRRs) were suggested by Pendry *et al.* in 1999 [16]. In addition to this, the first experimental results of composite metamaterials (CMMs) were presented by Smith *et al.* [17,18]. Since then, composite metamaterials, which are left-handed materials composed of arrays of periodic SRRs and thin wires in one and two dimensions, have attracted a great amount of attention and have been used in several applications including cloaking [19], superlens [20] and magnetic resonance imaging (MRI) [21] due to their unique physical properties.

Metamaterials, which make a kind of artificially engineered materials, can have negative effective permittivity and/or negative effective permeability. Together with the capacitive properties, split ring resonators have improved magnetic response and, therefore, they can be used to obtain a negative permeability. Split ring resonator structures are shown in Figure 3.2. They consist of two rings with splits on opposite sides. These splits are placed on

opposite sides in order to increase the capacitance of the SRR. Moreover, a gap between the two rings provides an additional capacitance to the structure. On resonance, there is induced current flowing around the rings.

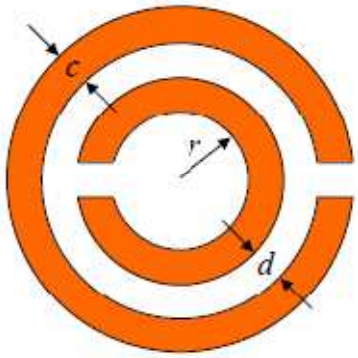

Figure 3.2 Split ring resonator structure proposed by Pendry *et al.*

While the negative permeability can be achieved with the periodic arrangement of the SRR structures, a single SRR can be used as a resonator thanks to its strong magnetic response. The idea of a single SRR and its working mechanism was first explained by Marqu´es *et al.* [22]. They have considered SRR as an L-C circuit that is driven by an external source. With the presence of metal rings, splits and gap, SRR structure can be accepted as an L-C circuit such that metal rings provide inductance, while the gap between the rings and splits in the rings provide capacitance. The important amount of the capacitance stems from the presence of the gap between the two rings [23]. SRR response to the time harmonic field can be explained by local field approach according to the idea of Marqu´es *et al.* that the application of a time varying magnetic field along the axis of SRR induces a current around the rings. Some of this induced current flows through the gap between the rings in the form of displacement current and some of it causes electrical charges to accumulate near the splits of the SRR.

When the SRR is classified as a resonator structure, diameter of the SRR is found to be nearly equal to the one tenth of the resonance wavelength ($2r \approx \lambda/10$)

[16]. Since the dimensions of the SRR are much shorter than the resonance wavelength of the structure, comparison of the dimensions with conventional resonator structures shows that SRR structure can be accepted as a sub-wavelength resonator with very compact dimensions. It is important to remember that two splits in the rings and a gap between the rings are the main source of the resonance at wavelengths much larger than the diameter of the rings.

When the SRR structure resonates, there occurs a dip in the transmission spectrum. This means that the resonance frequency (ω_0) of the SRR is the frequency of the dip in S_{21} graphs and it can be calculated from (4) [22]:

$$\omega_0 = \sqrt{\frac{2}{\pi r_0 L C_{pul}}} \tag{4}$$

where r_0 is the average radius of the SRR, L is the total inductance of the rings and C_{pul} is the per-unit-length capacitance between the rings. When the radius is in m, the capacitance per unit length is in F/m and inductance is in H, the resonance frequency is found to be in rad/s. To obtain this relation, the total capacitance of the SRR structure is considered to be the sum of the series capacitance of the upper and lower halves.

Various types of split ring resonators have been proposed in the literature. One type of split ring resonators is a complementary split ring resonator (CSRR) that is proposed as a counter part of the conventional SRR [24,25]. By using the idea of duality and Babinet's principle, instead of placing metal patterns for SRR, etching is applied to the metal sheet to construct the CSRR structure. Therefore, SRR and CSRR can be accepted as negative images and dual counterparts of each other. Moreover, it can be understood by using the duality principle that the electric field parallel to the axis of CSRR should be applied for the resonance of the CSRR structure. In addition, periodic CSRR structures can be used to obtain negative dielectric permittivity according to the idea of duality.

Figure 3.3 Complementary split ring resonator (CSRR).

Another type of split ring resonators is a closed split ring resonator or closed ring resonator (CRR) structure suggested by Koschny *et al.* [26]. Closed ring resonator structures can be obtained by removing the splits in the rings of the SRR as shown in Figure 3.4. Since the removal of the splits causes a decrease in the capacitance of the structure, the resonance frequency of the CRR is higher than the resonance frequency of the SRR with the same dimensions.

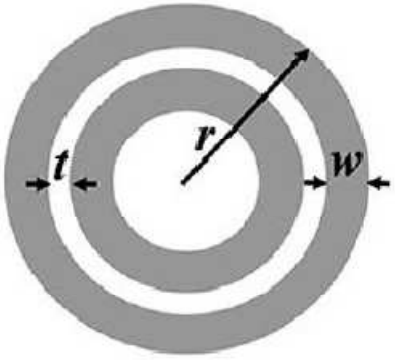

Figure 3.4 Closed ring resonator (CRR).

Broadside coupled split ring resonator (BCSRR) structure that was proposed by Marqu´es *et al.* [27] is another example of different types of SRR. BCSRR structure consists of two rings with equal radii on the two sides of the dielectric material. That is, the dielectric material is placed between the two rings of the SRR structure as shown in Figure 3.5.

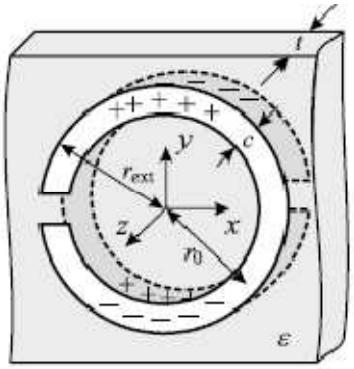

Figure 3.5 Broadside coupled split ring resonator (BCSRR).

Two other types of SRRs that are multi split ring resonators and comb-like split ring resonators are explained in detail in Sections 3.1 and 3.2.

3.1 Multi Split Ring Resonator

In some sensing applications, it is important to have a resonator with a low resonance frequency. However, the basic idea of increasing resonator dimensions to lower the resonance frequency is not very advantageous when the space for the sensor is limited. Therefore, some alternative ways to decrease the resonance frequency of the resonators have been worked on. Recently, it has been observed by Melik *et al.* that if the number of the rings in the SRR increases, the resonance frequency of the structure decreases [9]. According to this idea, addition of rings creates more gaps and, hence, the capacitance of the structure increases since the gaps in the resonator structure are the main source of the capacitance. With the increased capacitance, a reduction occurs in the resonance frequency of the structure according to (4). This means that a resonator with a lower resonance frequency can be obtained by multiplying the number of the rings in the classical split ring resonator structure. This split ring resonator structure that has a number of rings more than two can be named as a multi split ring resonator (MSRR).

As it can be seen from Figure 3.6, splits of the adjacent rings in the MSRR structure are placed on the opposite sides with respect to each other.

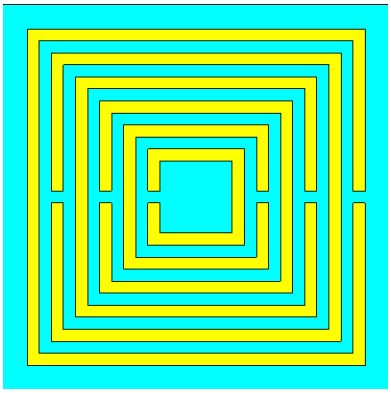

Figure 3.6 Multi split ring resonator.

3.2 Comb-Like Split Ring Resonator

In our study, we do not want to work at high frequencies due to the increased absorption rate. In addition, we do not prefer to work at low frequencies because the sensor dimensions increase with the increasing frequency. As a result, we select middle radio frequencies for our applications. We try to get a design with relatively low resonance frequency and small sensor size. Therefore, we do not use the basic idea of increasing resonator dimensions to lower the resonance frequency. A new architecture for the split ring resonators was proposed by Melik *et al.* in 2010 [9]. Since the idea of increasing the number of the rings in the SRR structure has resulted in the reduced resonance frequency, instead of adding new rings into the classical SRR, a number of pairs of teeth have been added into the split ring resonator with one outmost ring. This new SRR based structure shown in Figure 3.7 can be named as a comb-like split ring resonator structure because of its comb-like shape.

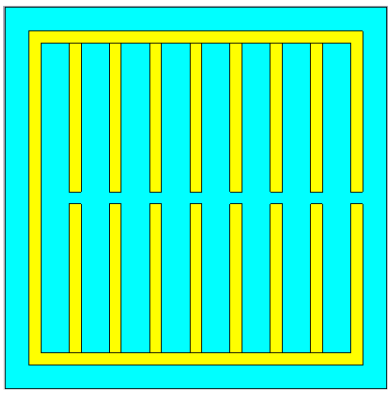

Figure 3.7 Comb-like split ring resonator.

This comb-like SRR structure has some more advantages when compared with classical SRR structure. First of all, it has a more compact design which consists of one ring resonator with a split and a number of pairs of teeth inside this one ring. Furthermore, the resonance frequency of the comb-like SRR is lower than the conventional SRR with the same dimensions. Due to the presence of a number of teeth pairs, this comb-like SRR structure has a lot of gaps, which provide high capacitance to the structure. As a result of its high capacitance value, comb-like SRR structure has a very low resonance frequency as expected.

The resonance frequency of the comb-like SRR structure heavily depends on the number of the teeth pair in the structure. When the number of the teeth pair in the structure increases, the number of the gaps also increases. While these changes result in an increase in the total capacitance, the resonance frequency of the comb-like SRR reduces as expected [9]. In other words, a comb-like SRR structure with a lower resonance frequency can be obtained by multiplying the number of the teeth in the structure.

The effects of the number of the rings in the multi SRR structure and the effects of the number of the teeth in the comb-like SRR structure can be observed in detail in Chapter 4 by examining the simulation results of these structures.

Chapter 4

Design Procedure

Properties of different types of split ring resonator structures including multi split ring resonators and comb-like split ring resonators have been studied in the previous chapter. By considering the advantages in the adjustment of the resonance frequency, multi split ring resonators and comb-like split ring resonators have been selected as the sensor candidate for our simulations. Therefore, simulations of multi SRR and comb-like SRR structures have been made to obtain the best resonator design for sensing applications.

We have started our work by determining the frequency range for our sensor designs. In order to make the experiments more easily, the radio frequency range of 3 Hz to 30 GHz has been selected at a first step. Since the absorption rate is very high at high frequencies and sensor dimensions are very big at low frequencies, we have preferred middle radio frequencies to obtain a sensor design with relatively low resonance frequency and small sensor size. Moreover, to have dimensions of sensors in a centimetre range, 400-450 MHz frequency range has been determined as the operating frequency of our sensors. This frequency range allowed us to avoid high frequency range where the intrinsic absorption of buildings increases. After the determination of the operating frequency range, related information in the literature has been searched. As a result of this literature search, it has been found that for a sensor that works at 400-450 MHz frequency, dimensions of the sensor should be nearly 5 cm. Resonance frequencies of various square shaped split ring resonator based designs with nearly 5 cm side length have been observed by making simulations of these structures using CST Microwave Studio. After making proper sensor designs by obtaining a large number of simulation results, designed sensors have

been fabricated and different types of experiments have been conducted with them.

4.1 Multi Split Ring Resonators

Rogers Duroid with a dielectric constant of 3.2, a loss tangent of 0.0045, and a thickness of 0.508 mm has been selected as a dielectric platform for both the simulations and fabrications of the multi SRR structures. The deposited metal on the Rogers Duroid for the patterning of the multi SRR design is a copper film with a thickness of 30 μm. Each gap width and each ring width has been decided to be 0.8 mm due to fabrication constraints.

Two waveguide ports at a sufficient distance away from the multi SRR structure have been constructed for the simulations as shown in Figure 4.1. While 0-10 GHz range has been selected as the frequency range for the simulations of multi SRRs with fewer rings, 0-800 MHz range has been selected as the frequency range for the simulations of multi SRRs with a larger number of rings. By using proper boundary conditions, the magnetic field has been defined to be perpendicular to the multi SRR plane and the electric field has been defined to be along the gap of the multi SRR structure. Time domain solver of the CST Microwave Studio has been used for the simulations of the multi SRR designs. S_{21} graphs of the simulations have been observed to determine the resonance frequency of the designed structures.

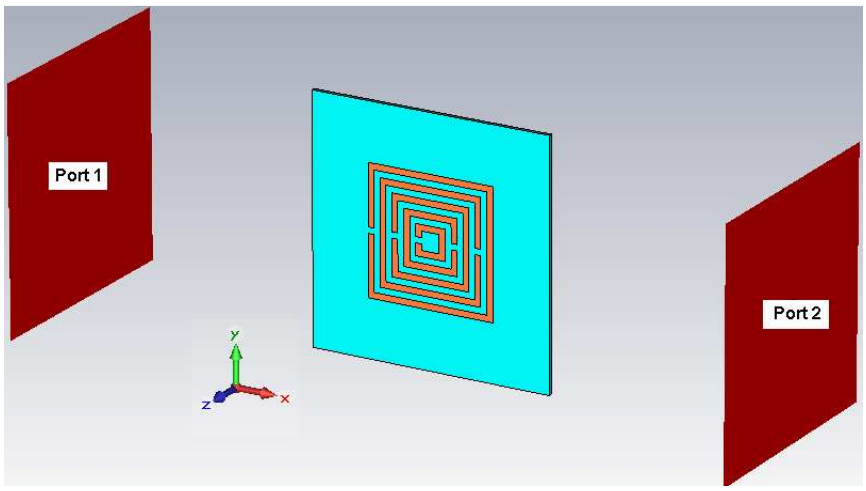

Figure 4.1 Simulation setup of multi SRR (H field in z direction, E field in y direction).

Simulations have been started with one ring resonator with a split as shown in Figure 4.2. Following this, number of the rings in the SRR structure has been increased such that splits of the adjacent rings have been placed on opposite sides with respect to each other. At each design step, one more ring has been placed outside and S_{21} responses of the simulations have been examined to determine the resonance frequency of the multi SRR structure. It is clear from the simulation results that as the number of the rings in the multi SRR structure increases, the resonance frequency of the multi SRR decreases as explained in Chapter 3. This shows that a multi SRR with more rings has a smaller resonance frequency as it can be seen from Table 4.1.

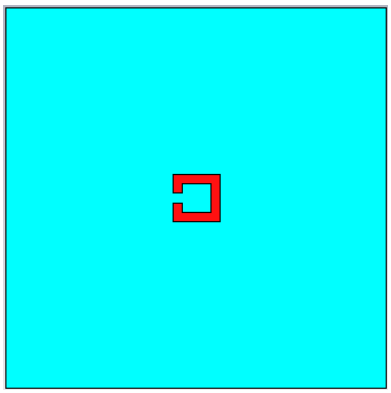

Figure 4.2 Multi SRR structure with one ring for the starting simulation (one ring resonator).

Number of the rings in multi SRR	Resonance Frequency of multi SRR
1	9.130 GHz
2	4.480 GHz
3	2.655 GHz
4	1.794 GHz
5	1.311 GHz
6	1.011 GHz
7	810.0 MHz
8	670.4 MHz
9	567.2 MHz
10	488.8 MHz
11	425.6 MHz
12	376.0 MHz

Table 4.1 Resonance frequencies and number of the rings of multi SRR.

After all of these simulation steps, a multi SRR structure with 11 rings has been designed. This multi SRR structure with 11 rings shown in Figure 4.3 has a resonance frequency of 425.6 MHz. Our designed multi SRR structure is in a square shape with the biggest ring side length of 36 mm and the dielectric side length of 37.6 mm. Each ring and each gap in our designed multi SRR structure has a 0.8 mm width.

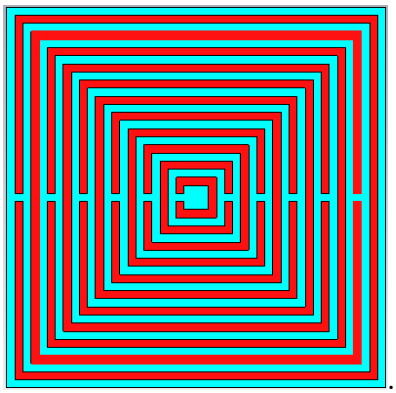

Figure 4.3 Designed multi SRR structure with 11 rings.

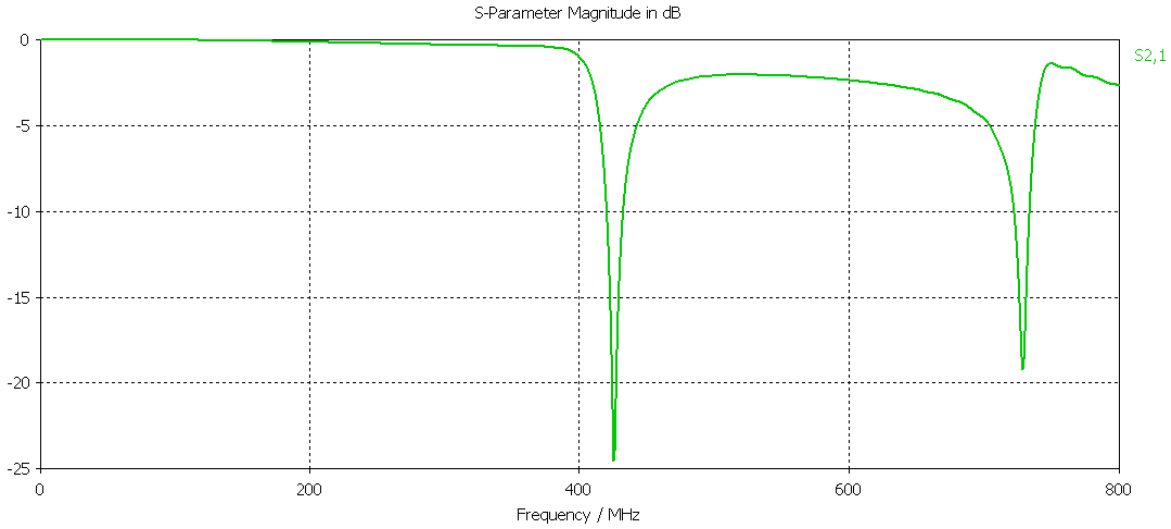

Figure 4.4 Magnitude of S_{21} vs. frequency of designed multi SRR with a resonance frequency of 425.6 MHz.

4.2 Comb-Like Split Ring Resonators

Rogers Duroid with a dielectric constant of 3.2, a loss tangent of 0.0045 and a thickness of 0.508 mm has also been selected as the dielectric for both the simulations and fabrications of our comb-like SRR structures. Copper with a film thickness of 30 μm has been used for the metal patterning of the comb-like SRR design. Each tooth length has been taken as 21.6 mm. Furthermore, each tooth width has been determined to be 0.8 mm due to fabrication constraints.

Similar to multi SRR case, two waveguide ports at a sufficient distance away from the comb-like SRR structure have been constructed for the simulations as shown in Figure 4.5. 0-800 MHz range has been selected as the frequency range of our simulations. By using proper boundary conditions, magnetic field has been defined to be perpendicular to the comb-like SRR plane and electric field has been defined to be along the gap of the comb-like SRR structure. Again, time domain solver of the CST Microwave Studio has been used for the simulations of these designs. S_{21} graphs of the simulations have been observed to determine the resonance frequency of the designed comb-like SRR structures.

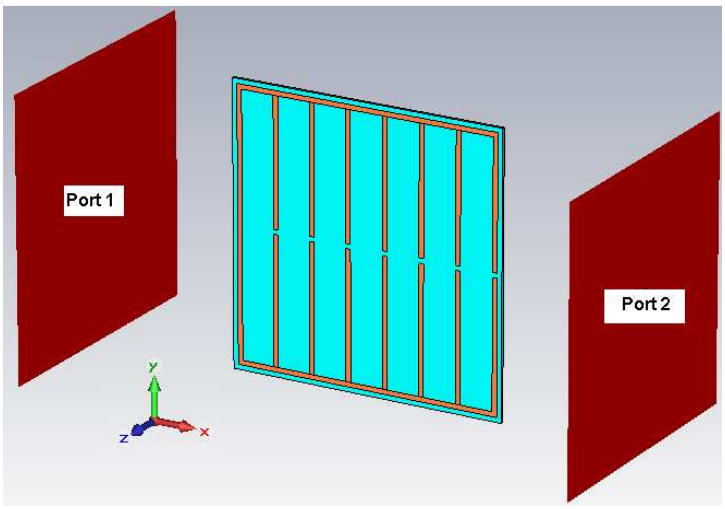

Figure 4.5 Simulation setup of comb-like SRR (H field in z direction, E field in y direction).

A comb-like SRR structure with no teeth on one side has been simulated at the first step as shown in Figure 4.6. After simulating this comb-like SRR with only one ring, to find the effects of the number of teeth on the resonance frequency, the teeth number in the comb-like SRR structure has been increased. Resonance frequencies of the comb-like SRRs have been determined by observing the S_{21} responses of the simulations. By examining the simulation results, it can be concluded that as the number of the teeth pair in the comb-like SRR increases, the resonance frequency of the structure decreases as discussed in the theoretical information in Chapter 3. In other words, so as to have a comb-like SRR design with a smaller resonance frequency, the number of teeth in the comb-like SRR structure should be increased. Resonance frequency and number of teeth pair relationship can be understood from Table 4.2.

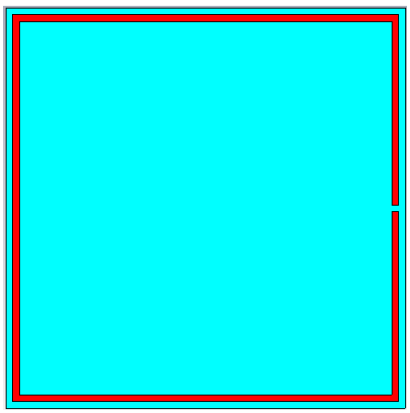

Figure 4.6 First simulated comb-like SRR structure with one ring (one ring resonator).

Total number of the teeth of comb-like SRR	Resonance Frequency of comb-like SRR
0	636.8 MHz
2	583.2 MHz
4	548.0 MHz
4(*)	546.4 MHz
4(*)	543.2 MHz
4(*)	540.0 MHz
6	519.2 MHz
6(*)	515.2 MHz
8	496.8 MHz
10	482.4 MHz
12	472.8 MHz
16	456.8 MHz
26	428.8 MHz
54	402.4 MHz

Table 4.2 Number of teeth pair and resonance frequency relationship for a comb-like SRR.

(*) for non-symmetric teeth distribution

As a result, with the addition of 27 teeth pair to the starting ring resonator structure, the desired comb-like SRR structure with a resonance frequency of 402.4 MHz has been designed. This implies that a total of 54 teeth have been inserted into the one ring resonator to get a comb-like SRR structure that resonates at 402.4 MHz. Our designed comb-like SRR structure is in a square shape with a metal pattern side length of 45.6 mm and a dielectric side length of 47.2 mm. Each tooth in the comb-like SRR structure has a 21.6 mm length and a 0.8 mm width. The width of each gap in the comb is also 0.8 mm.

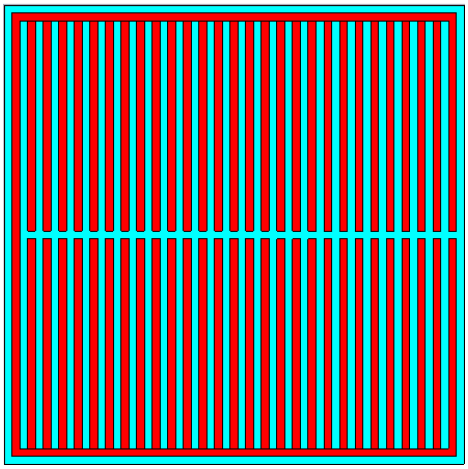

Figure 4.7 Designed comb-like SRR structure with a total of 54 teeth.

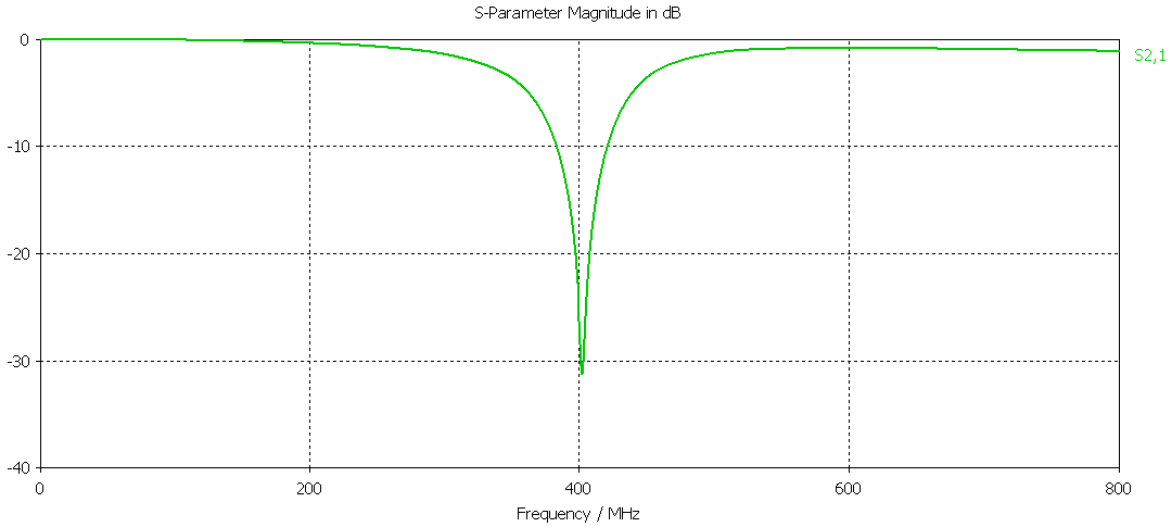

Figure 4.8 Magnitude of S_{21} vs. frequency of our designed comb-like SRR with a resonance frequency of 402.4 MHz.

4.3 Antenna

In telemetric sensing applications, the sensitivity of an external antenna to tiny variations can be improved by narrowing the bandwidth of the antenna. Therefore, in order to observe small changes and determine the response of the sensor more accurately, it is better to use an antenna with a narrow bandwidth. Since loop antennas have narrower bandwidths relative to the other types of the

antennas, they can be suitable for sensing applications. Moreover, using loop antennas for sensing applications is very advantageous because loop antennas are inexpensive and easy to construct. In addition to this, for the ease of experiments, usage of a printed antenna, which is more durable and stable, is very crucial. That is to say, to have narrow bandwidth, compact design, high ruggedness and low cost, we have considered to use a printed loop antenna for our experiments in this work.

For frequencies up to 3 GHz, loop antennas are very suitable choices among different types of antennas. Loop antennas have a low production cost and they are simple to design and build. They can have various shapes including triangle, rectangle, circle, ellipse, square, etc. They can be classified into two groups with respect to their sizes. A loop antenna can be named as electrically small if it has a circumference smaller than one tenth of a wavelength. However, if a loop antenna's circumference is in the order of a wavelength it can be accepted as electrically large [28].

Literature search has been undertaken as a first step for the design of a printed loop antenna which works at the frequency close to the resonance frequencies of our designed sensors. Various approaches and associated formulae to design a loop antenna from a wire have been suggested, yet there is not much information to design a printed loop antenna. Therefore, a formula suitable for wire loop antennas is used to design a printed loop antenna as the starting point. Radiation resistance of a one turn loop antenna can be found in (5), but remember that this is suitable for the wire loop antennas and not printed ones [28]:

$$R_r \simeq 31171 \left(\frac{S^2}{\lambda^4}\right) \quad \Omega \tag{5}$$

where S is the area of the loop antenna in m^2 and λ is the wavelength in m.

For a given frequency and a radiation resistance, the required diameter of a wire loop antenna can be determined from (5). When the frequency is determined, the wavelength (λ) in m is, simply,

$$\lambda = \frac{c}{f} \tag{6}$$

where c is the velocity of a wave ($c = 3 \times 10^8$ m/s) in free space and f is the operating frequency in Hz.

In our case, the frequency is selected as 420 MHz and, thus, the wavelength is found to be 71.43 cm. The radiation resistance (R_r) is selected as 50 Ohm since all coaxial cables and connectors have 50 Ohm impedance. Therefore, while a square shaped loop antenna with 50 Ohm radiation resistance at 420 MHz frequency should have a side length of 14.29 cm, a circular loop antenna with 50 Ohm radiation resistance at 420 MHz frequency is required to have a diameter of 16.13 cm. For the starting design of a printed loop antenna, the radius parameter is considered as if it is a wire loop antenna at the beginning.

Simulations for the design of a printed loop antenna have been performed using CST Microwave Studio. Time domain solver of the CST Microwave Studio has again been used for simulations. Different mesh sizes have been tried for simulations and the most suitable mesh size for both time and accuracy has been considered. Accuracy has been determined by looking at the simulation results with smaller mesh sizes. If a simulation result with a bigger mesh size is very close to the simulation result of a smaller mesh size and it takes much less time for the bigger mesh size simulation to finish, the simulation with the bigger mesh size has been chosen.

In the simulation results, S_{11} parameter graphs and Smith charts of the loop antenna have been investigated. In order to determine the proper antenna design that has a result in the 1±jx circle at 420 MHz frequency, looking at Smith chart results of the simulations is crucial. So as to match the radiation resistance of the

antenna to 50 Ohm at 420 MHz frequency by using additional capacitances and inductances, Smith chart data gives a valuable insight.

For the printed loop antenna, Rogers Duroid is selected as the dielectric substrate. Rogers Duroid with a dielectric constant of 3.2, a loss tangent of 0.0045, and a thickness of 0.508 mm is again used for both the simulations and fabrication of the antenna. Copper with a film thickness of 30 μm is also used for the metal patterning of the printed loop antenna.

By using the radiation resistance (5), the circularly shaped loop antenna's diameter has been found to be 16.13 cm while the square shaped loop antenna's one side has previously been found to be 14.29 cm. It is important to remember that shape of the loop antenna does not have any significance on the electrical characteristics of the antenna. Electrical properties such as radiation pattern and radiation resistance only depend on the loop area. Therefore, for practical concerns in the production level, instead of a circular shape, a square shaped loop antenna has been selected for our work. However, with the consideration of the differences between wire and printed antennas, one side of the square antenna has been selected a little different from 14.29 cm for the first step of the simulations. A square shaped loop antenna with a 17 cm outer side length has been constructed with a copper pattern on the Rogers Duroid as shown in Figure 4.9. In order to start a design, the metal width of the loop has been selected as 2 mm. A dielectric substrate that is also in square shape has been used with a 20 cm side length. Simulation result of the first design is shown in Figure 4.10.

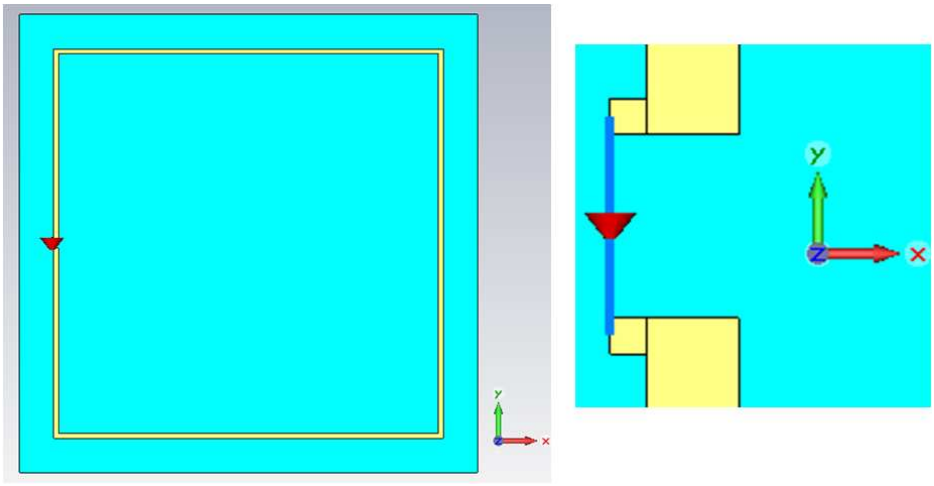

Figure 4.9 (a) First simulated printed square loop antenna and (b) discrete port with 50 Ohm impedance used for simulations.

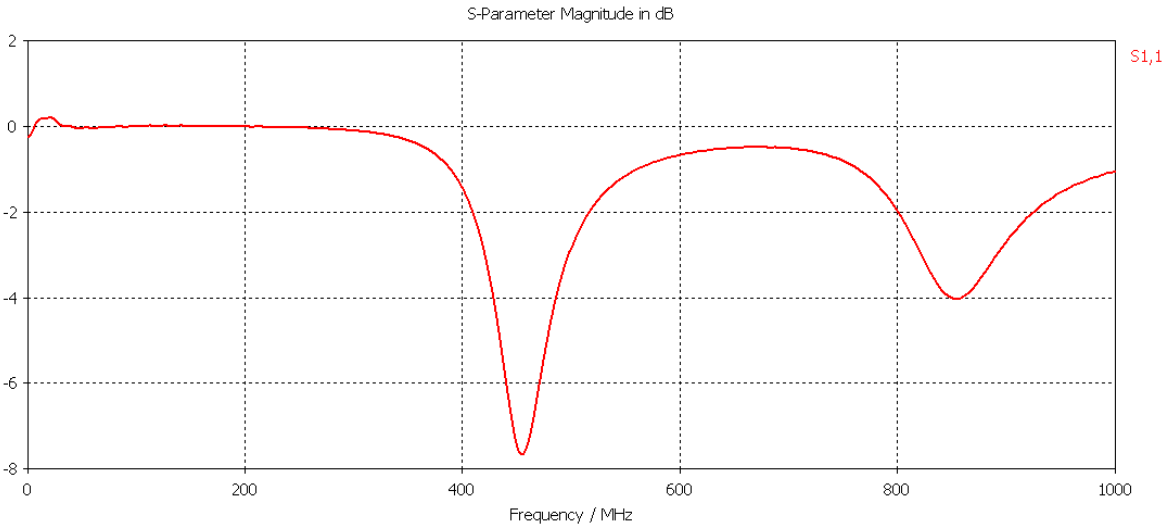

Figure 4.10 Magnitude of S_{11} vs. frequency of the first design with a resonance frequency of 455 MHz.

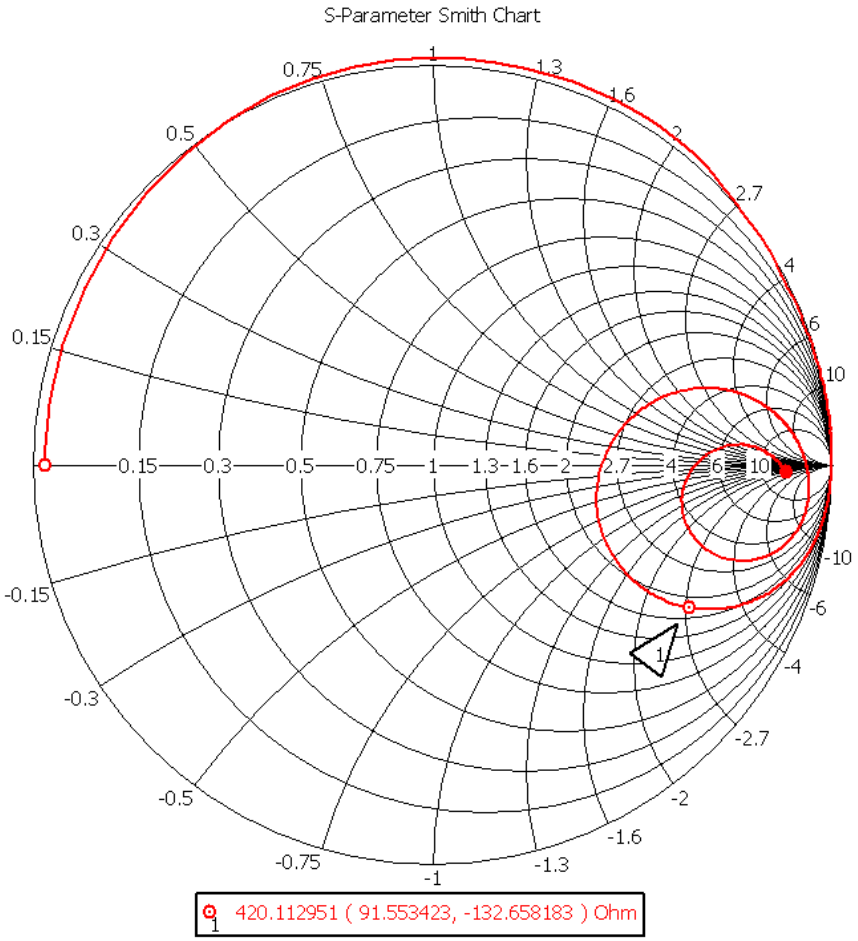

Figure 4.11 Smith chart plot of the first design.

To apply matching techniques to the antenna, addition of parallel capacitance and series inductance has been preferred because of the ease in fabrication since matching with an additional parallel inductance seems complicated in this step. Required values for the additional parallel capacitances and series inductances are calculated using the matching techniques and these values are checked by using a software application called Super Smith 2.07.

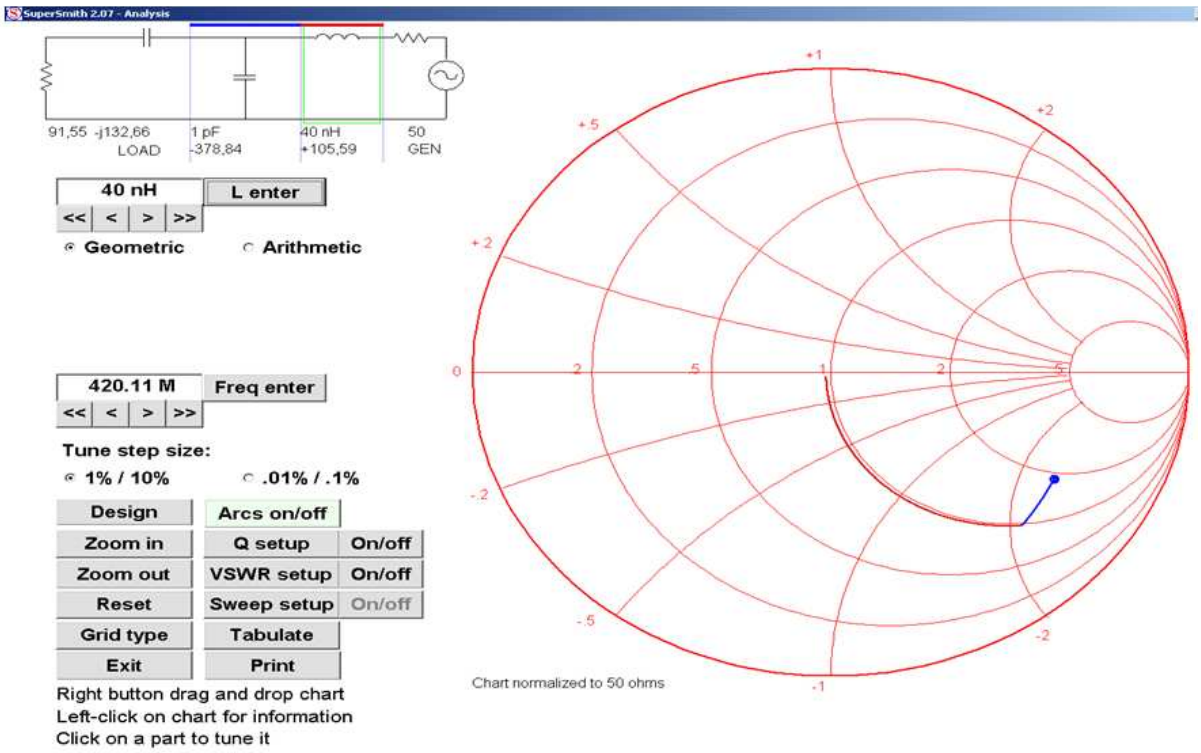

Figure 4.12 Matching control of the antenna using Super Smith 2.07.

Lumped capacitor element has been used for both the simulations and fabrications. Design of an additional printed inductor has been made by using the modified form of Meander inductor (7) [29]. This can be used to find the inductance of a strip as follows:

$$L = 0.2 \times l \times \left[\ln\left(\frac{2\times l}{W+H}\right) + 0.2235 \times \left(\frac{W+H}{l}\right) + 0.5\right] \; nH \qquad (7)$$

where l is the length of the trace, W is the width of the trace, H is the height of the trace, and all dimensions are in millimetre. We can see here that, if the strip length increases, inductance also increases.

Following these steps, the set values of printed inductor and lumped capacitor have been added to the antenna design and simulations have been repeated. As a result, a square shaped printed loop antenna with 50 Ohm radiation resistance at 420 MHz frequency has been designed as shown in Figure 4.13. Smith chart

result given in Figure 4.15 also shows that the applied matching has a very good result at 420 MHz frequency.

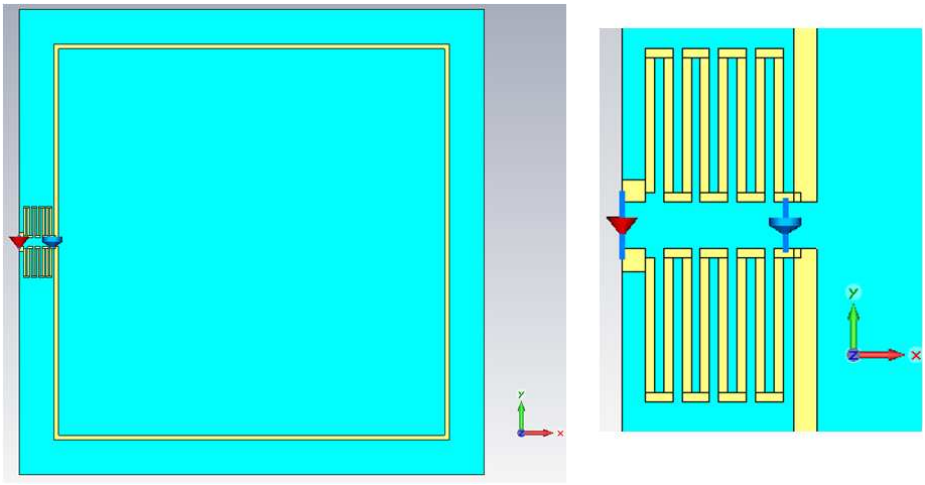

Figure 4.13 (a) Final design of a printed square loop antenna and (b) discrete port with 50 Ohm impedance and 0.7 pF parallel capacitance are used for simulations.

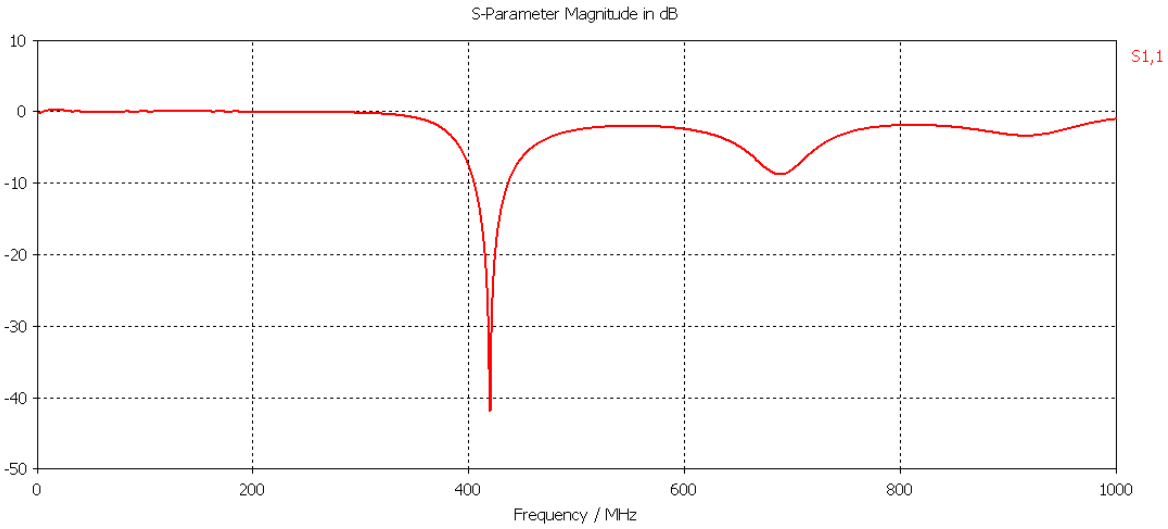

Figure 4.14 Magnitude of S_{11} vs. frequency graph of our designed loop antenna with a resonance frequency of 420 MHz.

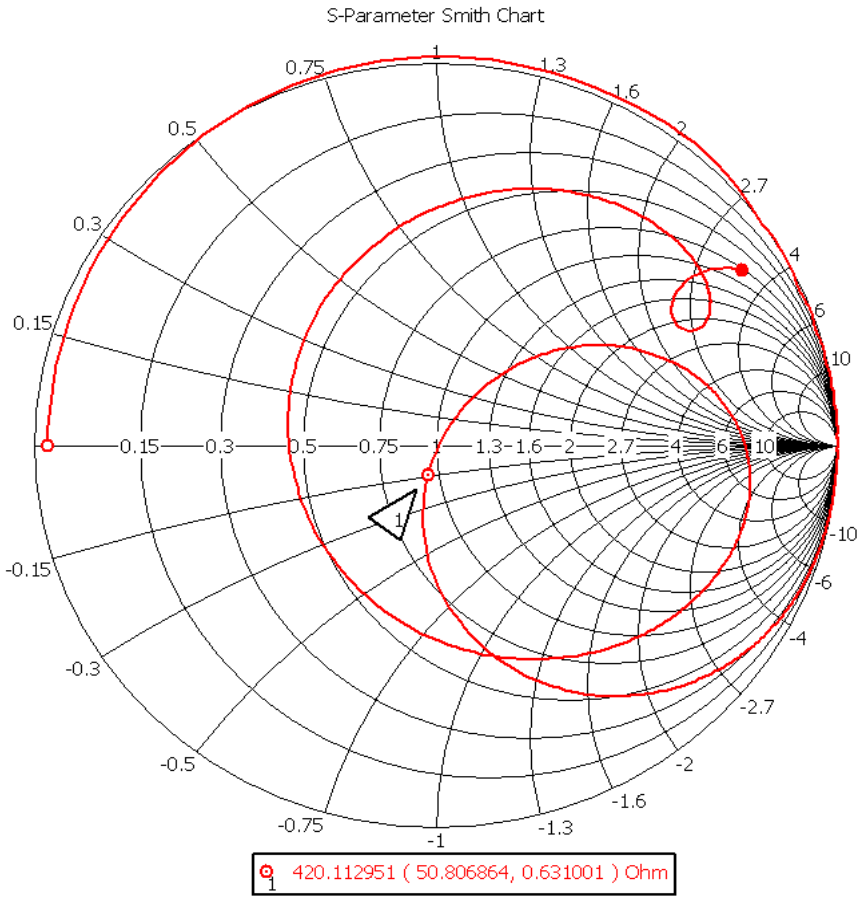

Figure 4.15 Smith chart plot of the final design.

4.4 Antenna and Comb-Like SRR

After completing the design steps of the comb-like SRR and printed square shaped loop antenna structures separately, the full simulation setup with both the comb-like SRR and printed loop antenna has been constructed in CST Microwave Studio. As before, time domain solver of the CST Microwave Studio has been used for the simulation of the full setup. Mesh sizes for the structures have been selected as in the previous separate simulations.

Since the power in our experiments is limited with the network analyzer output, we have set the distance between the antenna and comb-like SRR as 15

cm. This means that for practical purposes, the distance between the antenna and comb-like SRR has been determined to be 15 cm in all simulations and experiments in this work. Therefore, our comb-like SRR structure has been placed at 15 cm away from the printed loop antenna as shown in Figure 4.16.

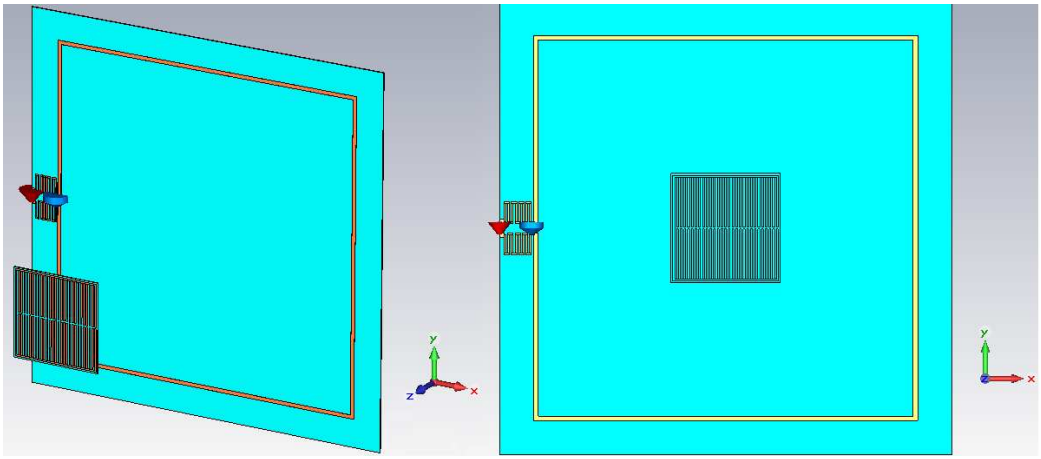

Figure 4.16 Full simulation setup: (a) perspective view and (b) front view.

It is important to note that in order to have an uncoupled system, the structure should be placed in the far field region of the antenna. Therefore, the distance between the antenna and comb-like SRR structure should be greater than the wavelength to obtain an uncoupled system. The resonance frequency of our printed loop antenna is 420 MHz and the resulting wavelength is 71.43 cm for this frequency as calculated previously. Therefore, so as to get an uncoupled system, the distance between our designed comb-like SRR sensor and printed square shaped loop antenna should be greater than 71.43 cm. However, since the distance between the antenna and comb-like SRR is 15 cm which is much less than 71.43 cm, our designed full system is coupled for the simulation. The result in Figure 4.17 has been obtained from the simulation of the full system.

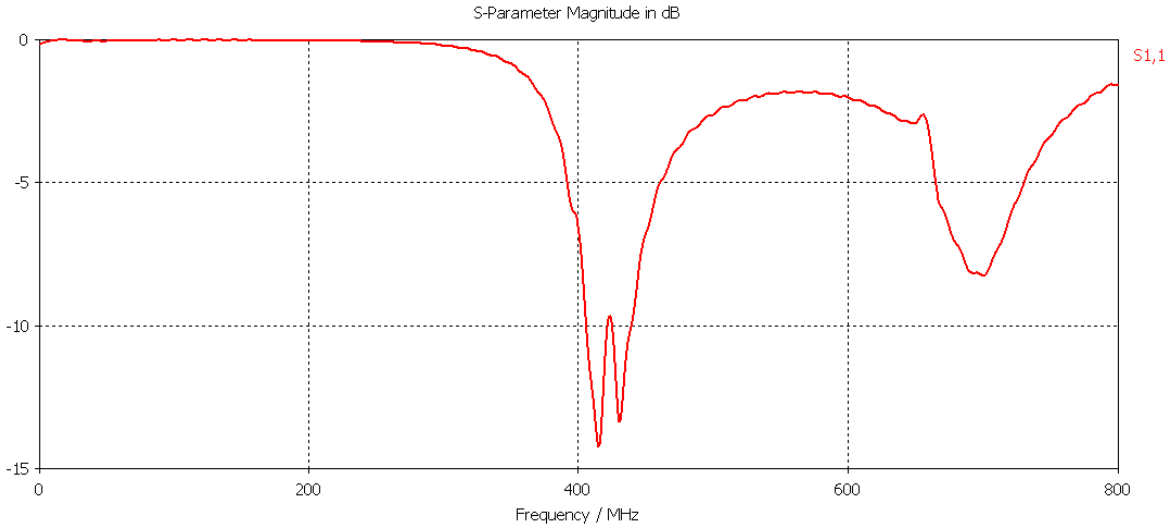

Figure 4.17 Magnitude of S_{11} vs Frequency graph of the full system simulation.

Chapter 5

Experiments

To evaluate the sensor and antenna performance, different types of experiments have been conducted. One port S-parameter (S_{11}) characteristics have been recorded during these experiments and these measurements have been evaluated to verify the theoretical and simulation results.

5.1 Theoretical Background

Scattering parameters can be named as S-parameters in shorthand notation. They are used to define the characteristics of linear electrical networks at radio and microwave frequencies. S-parameters are valuable when determining the related information, e.g., about return loss, gain, voltage standing wave ratio, and stability of amplifiers [30].

For the two-port network configuration shown in Figure 5.1, normalized incident power waves at port i are shown with a_i, normalized reflected power waves at port i are shown with b_i (i=1,2).

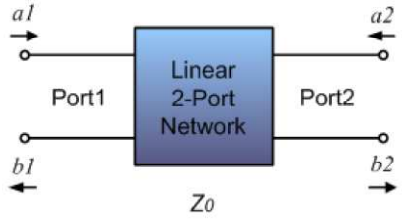

Figure 5.1 Two port network, where a_1 is incident power and b_1 is reflected power at port 1, and a_2 is incident power and b_2 is reflected power at port 2.

The matrix given by (8) is called S-parameter matrix and is useful to determine the relationship between the incident and reflected levels of power at each port. S_{11} and S_{22} can be used to find voltage standing wave ratio (VSWR), while S_{21} and S_{12} can be used to find gains and attenuations.

$$\begin{pmatrix} b1 \\ b2 \end{pmatrix} = \begin{bmatrix} S11 & S12 \\ S21 & S22 \end{bmatrix} \begin{pmatrix} a1 \\ a2 \end{pmatrix} \quad (8)$$

$S_{11} = \frac{b1}{a1}$ shows the input reflection coefficient when a_2=0,

$S_{21} = \frac{b2}{a1}$ shows the forward transmission coefficient when a_2=0,

$S_{12} = \frac{b1}{a2}$ shows the reverse transmission coefficient when a_1=0, and

$S_{22} = \frac{b2}{a2}$ shows the output reflection coefficient when a_1=0.

Since our designed printed loop antenna has been modeled as a one port device, only the input reflection coefficient (S_{11}) can be measured during our experiments in this work.

5.2 Experimental Procedure

HP Agilent E5071C ENA Network Analyzer, which allows measurement within the frequency range 300 KHz-20 GHz, has been used for all experiments in this work.

Figure 5.2 HP Agilent E5071C ENA Network Analyzer.

Before the measurement of S_{11}, one port calibration of the network analyzer has been performed by using the calibration kit to prevent errors in the measurements. The network analyzer is calibrated at the end of the coaxial cable where it is connected to the printed loop antenna.

Calibration kit has there ports for OPEN, SHORT and LOAD calibration cases and one port calibration has the following steps:

- Set the frequency range: Adjust the frequency range of the measurements according to the experiment. In our experiments, 350 MHz-500 MHz frequency range has been selected.
- Set the IF bandwidth: For the measurements, adjust IF bandwidth carefully. In our experiments, IF bandwidth has been determined as 10 KHz.
- Set power level: Set power level according to the experiment conditions. In our experiments, the power is set to 10 dBm, which is the highest level of the network analyzer output.
- Set number of points: For the measurements, adjust number of points accordingly. In our experiments, the number of data points has been selected as 1601, which is the highest level of the network analyzer. This implies that 1601 test points have been collected in the 350-500 MHz range.

After making these adjustments, one port calibration has been selected from the network analyzer control panel. Then, a coaxial cable (UTiFLEX Flexible Microwave Cable Assemblies UFA147B) suitable for radio frequencies has been connected to the selected port of the network analyzer. Calibration kit has been fastened to the end of the coaxial cable, and OPEN, SHORT, and LOAD steps of the calibration have been performed.

With the help of a network analyzer, the real and imaginary parts (or, magnitude and phase) of the S-parameters can be obtained. For our case, we have used the magnitude of S_{11} data to evaluate our experimental results. Since impedance of the antenna can be obtained and matching can be controlled by

using the Smith chart, to check the radiation resistance and matching of our printed loop antenna, we have used the Smith chart plots at the desired frequency. Moreover, we have used an additional matching network for the tuning of the antenna to obtain maximum power transfer at a single frequency when the antenna did not exhibit a desired resonance frequency.

5.3 Experiment Sets

All design steps of the multi SRR, comb-like SRR, and printed square shaped loop antenna structures are explained in Chapter 4. After completing the simulations of these structures separately, the full setup with both the comb-like SRR and printed loop antenna has been simulated as a last step of the design part. Subsequently, our designed multi SRR, comb-like SRR and printed square shaped loop antenna structures have been fabricated. These multi SRR, comb-like SRR and printed square shaped loop antenna structures shown in Figures 5.3, 5.4 and 5.5 have then been used in our experiments.

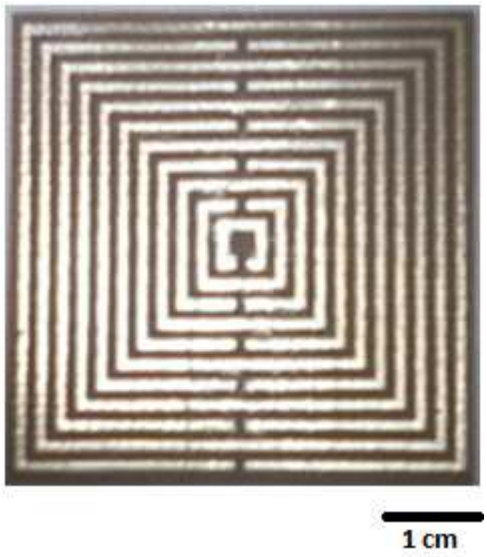

Figure 5.3 Fabricated multi SRR.

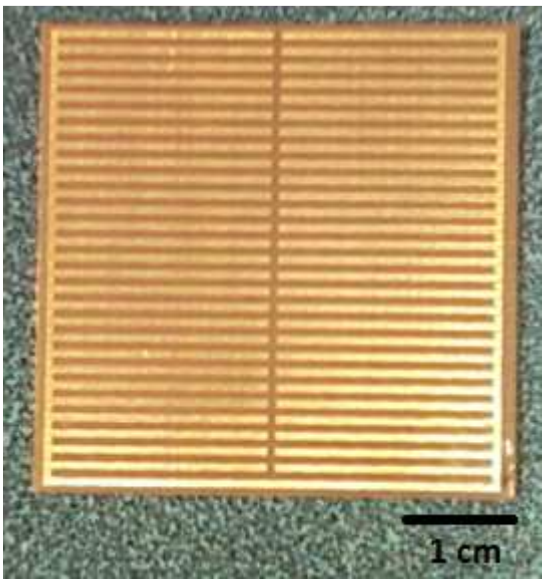

Figure 5.4 Fabricated comb-like SRR.

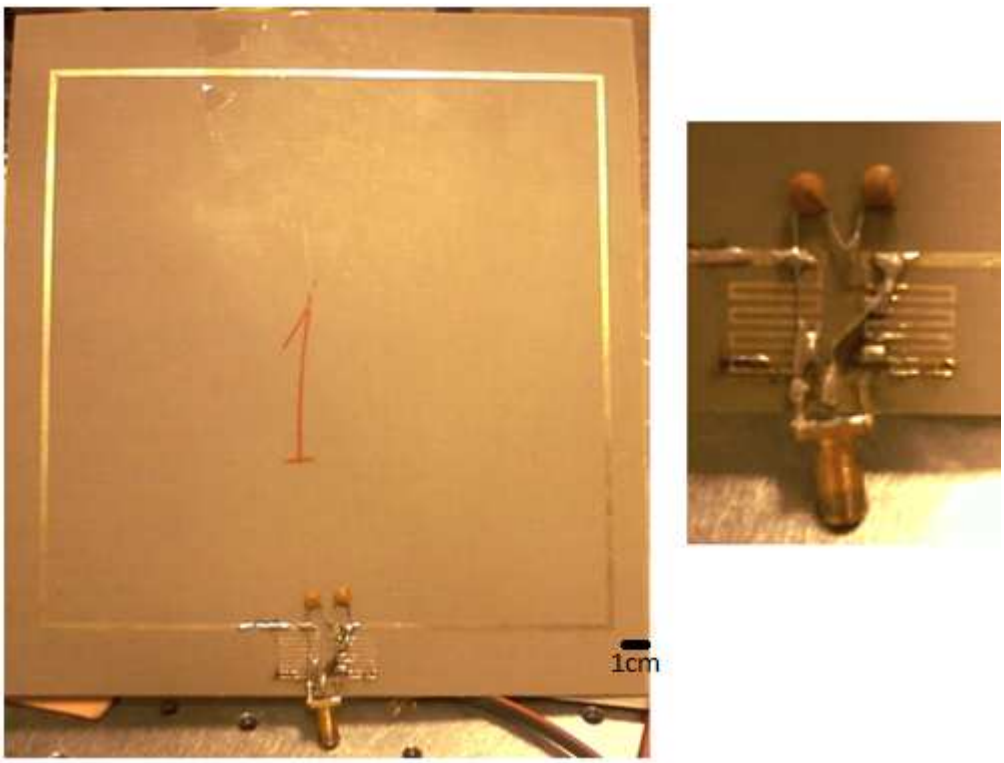

Figure 5.5 (a) Fabricated square shaped printed loop antenna along with (b) its 0.5 pF capacitor and printed inductor used for the matching of the antenna.

Before starting any sensing experiment, antenna matching has been checked and the frequency response of the comb-like SRR has been controlled. First of all, frequency response of the fabricated printed loop antenna has been observed by looking at the S_{11} graph to determine the resonance frequency. Calibration steps have been performed as previously described. Figure 5.6 shows the experimental characterization of the printed square shaped loop antenna at a resonance frequency of 419.5 MHz, which is very close to our simulation result of 420 MHz.

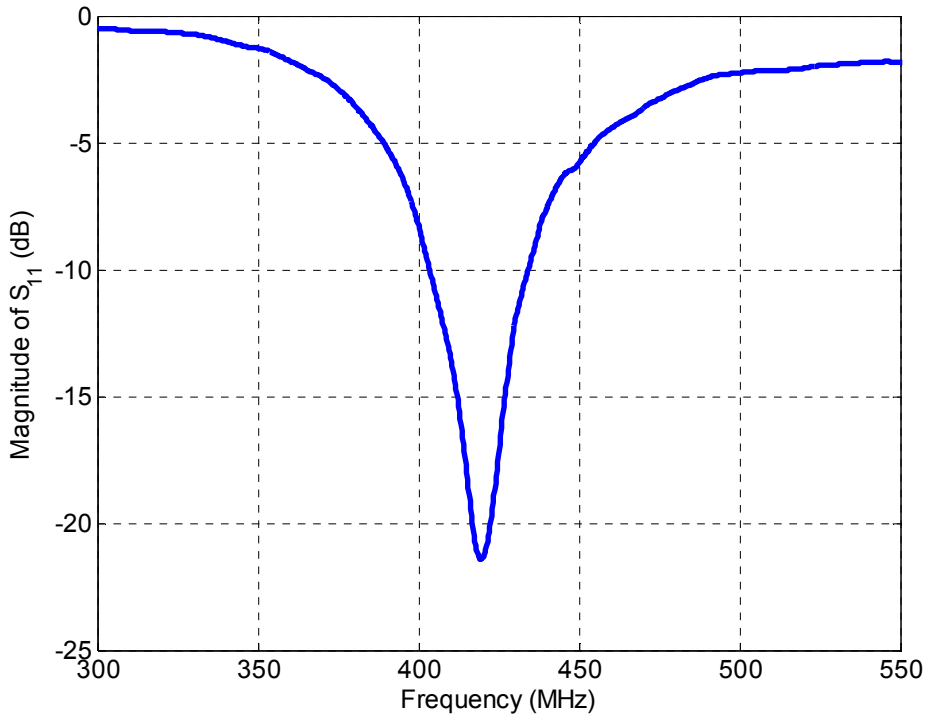

Figure 5.6 Frequency response of the fabricated printed loop antenna.

After the characterization of the printed loop antenna alone, the full apparatus including both the comb-like SRR and printed square shaped loop antenna has been constructed. For practical purposes, distance between our printed loop antenna and sensor has been determined to be 15 cm for all experiments in this work. Fabricated comb-like SRR sensor has been placed at 15 cm away from the

printed loop antenna so the coupled system has been obtained. Figure 5.7 shows the result of this experiment.

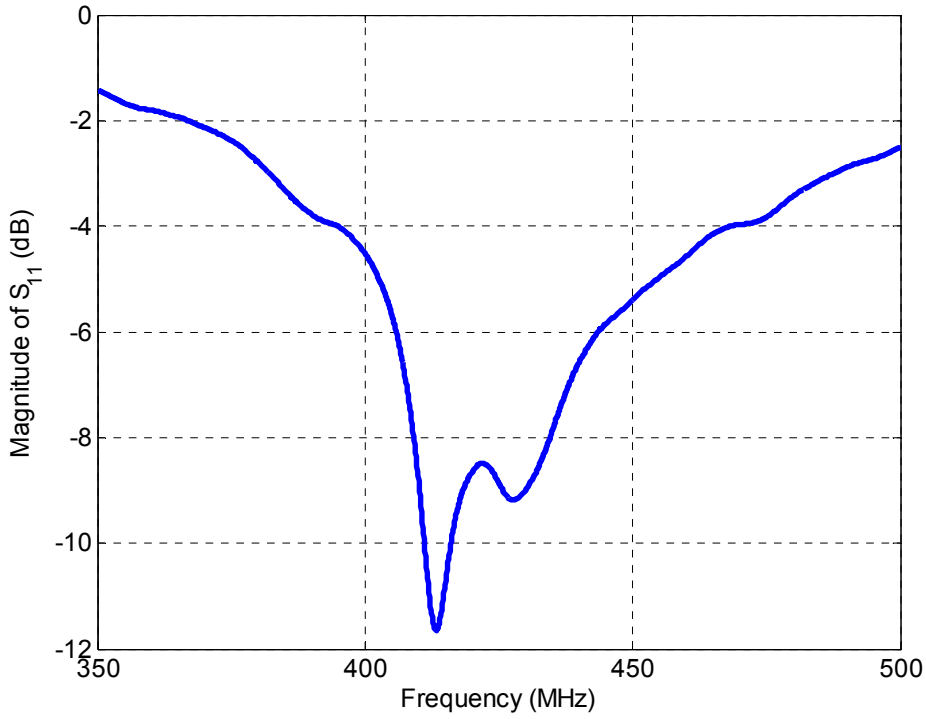

Figure 5.7 Frequency response of the full experimental setup using our comb-like SRR.

After these control experiments, different types of experiments have been conducted to evaluate the sensor performance under various conditions. As the first experiment, although the parts of a structure on which the proposed sensors are intended to be mounted are made of steel rods, the current experimental setup for a proof-of-concept study has been designed for controlled precise positioning of parts of the comb sensors. For this type of experiments, the variations in the sensor geometry due to an applied external force has been mimicked by moving the parts of the comb-like SRR structure, which provides a means of controlled change in the gap width of the comb-like SRR structure. After the first type of displacement experiments, the experimental apparatus for mechanical loading in a scaled-down version of a building has been used. Delrin with a Young modulus smaller than that of steel rods has been selected as the

deformable platform to induce strain easily and to ease the experiments using scaled-down external force levels. Therefore, the load has been applied to a platform made up of Delrin instead of steel rods. With the success of these two experiment types, as the last and the most important step, comb-like SRR sensor has been mounted on real steel rods and experiments have been conducted with a concrete in real environment by applying high levels of load to steel rods.

5.4 Error Criterion

To evaluate the designed comb-like SRR convenience for sensing applications, a linear relationship should preferably exist between the resonance frequency and the applied load amount or the displacement because linearity provides equal level of sensitivity throughout the dynamic range. Therefore, properties of the linearity between resonance frequency and the load amount or the displacement should be examined carefully.

Linearity of data points on an arbitrary curve can be determined by using various error criteria. After the application of a linear fit technique to arbitrary data points, goodness of the fitted line can be checked by looking at different statistical parameters: e.g., the sum of squares due to error (SSE), R-square, and root mean squared error (RMSE). In our work, R-square value of the fitted data has been used to determine the goodness of the linear fit.

The ratio of the sum of squares of the regression (SSR) to the total sum of squares (SST) can be identified as the R-square value. SSR, SST, and R-square are given by (9)-(11):

$$SSR = \sum_{i=1}^{n} w_i(\hat{y}_i - \bar{y})^2 \tag{9}$$

$$SST = \sum_{i=1}^{n} w_i(y_i - \bar{y})^2 \tag{10}$$

$$\text{R-square} = \frac{SSR}{SST} \tag{11}$$

where w_i is the weighting coefficient, y_i is the response value, $\hat{y}_i$ is the predicted response value, and $\bar{y}$ is the mean of the response values.

R-square value of the fitted data shows the success rate of a fit model in representing an original data. In other words, R-square value shows the square of the correlation between original values and fitted values. While the R-square value ranges between 0 and 1, a value that is close to 1 indicates a good agreement between the fitted model and original data. For instance, if the R-square value equals to 0.75, that means fitted model explains 75% of the total variation in the data on the average.

To determine the appropriateness of our design for sensing application, we have investigated the linearity of resonance frequency versus displacement and resonance frequency versus load level. For this purpose, linear fitting has been applied to the experimental results and R-square value of the fitted line has been quantified. For practical purposes, the minimum R-square value for the linearity check process has been taken at a high R-square value as 0.95. This means that, when the R-square value of the linear fitted curve of the original data points is greater than 0.95, the original data points are accepted as reasonably linear. In our experiments, if a linear fit of the resonance frequency versus displacement/load plots leads to a R-square value greater than 0.95, these original data points are practically considered to be linear with a small error value, and a linear relationship can be accepted between the resonance frequency and displacement/load. As a result, this comb-like SRR structure can be possibly used for sensing applications.

5.5 Displacement Experiments

The idea of a sensor relies on a principle that, as the strain changes in a structure, there occurs a displacement and a gap width changes in the comb-like SRR sensor that is placed on the deforming structure. In our work, the parts of a structure on which the proposed sensors are intended to be mounted are made of steel rods as used in buildings. However, experimental setup suitable for the application of the load to steel rods is complicated, hard to build and expensive. Therefore, the first experimental setup for a proof-of-concept study has been designed for controlled precise positioning of parts of the comb-like SRR sensors. For this purpose, the variation in the sensor geometry due to an applied external force is mimicked by intentionally displacing the comb-like SRR parts in a controlled manner. A xyz-stage shown in Figure 5.8 has been used to provide controlled positioning of the parts of our comb-like SRR sensor.

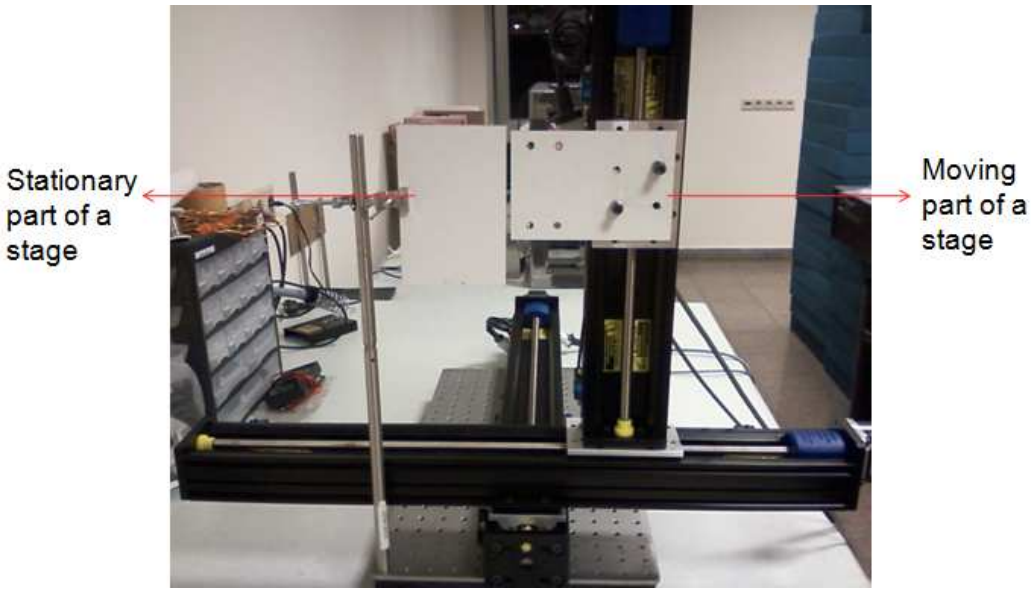

Figure 5.8 xyz-stage.

Our designed comb-like SRR sensor has been cut into two pieces from the gap between teeth. A nearly 2 cm long copper wire with a 0.2 mm diameter has

been soldered as a jumper to these two pieces to provide an electrical connection between them as shown in Figure 5.9.

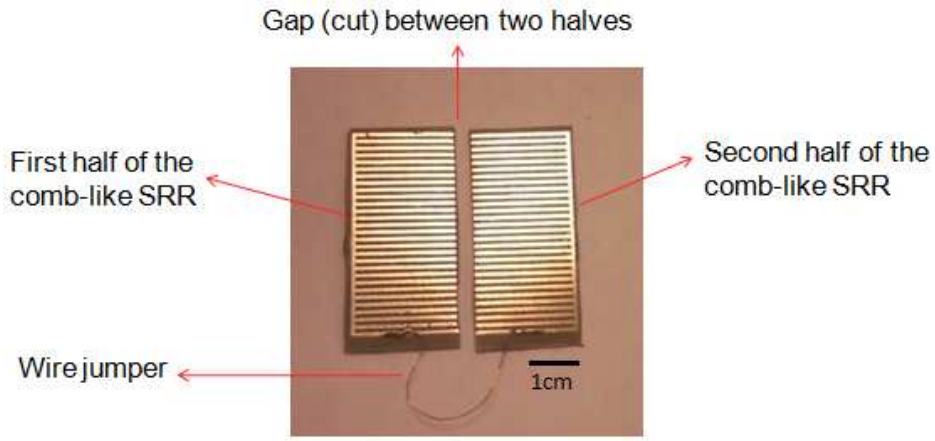

Figure 5.9 Two parts of the comb-like SRR structure connected with a copper wire jumper.

One part of the comb sensor has been fixed onto the stationary part and other part of the comb has been fixed to the moving part of the xyz-stage as shown in Figure 5.10.

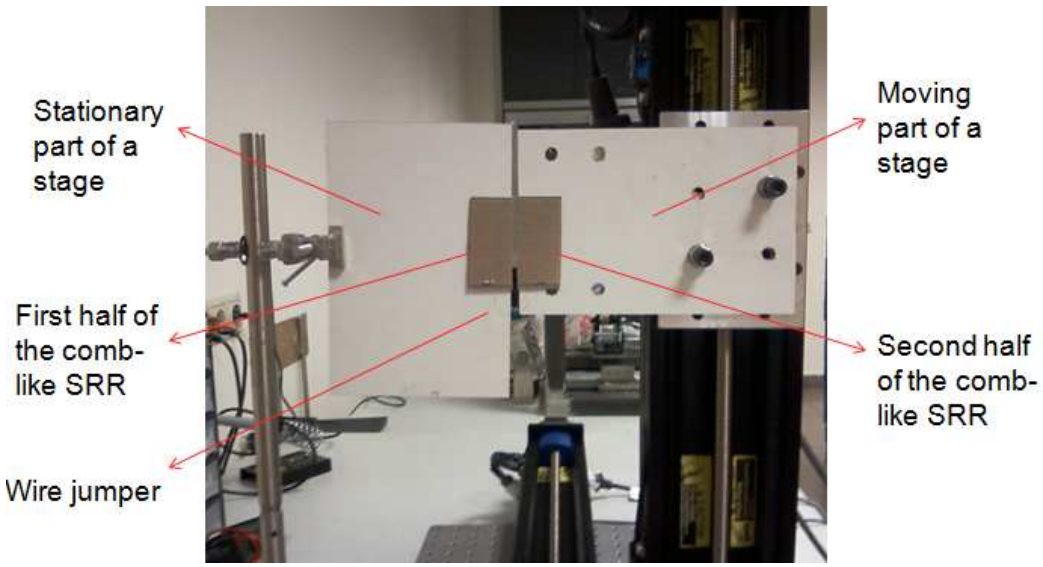

Figure 5.10 Stationary and moving parts of the stage with comb-like SRR parts.

A printed square shaped loop antenna connected to a calibrated network analyzer has been placed at 15 cm away from the comb-like SRR sensor and thus the full experiment setup in Figure 5.11 has again been constructed.

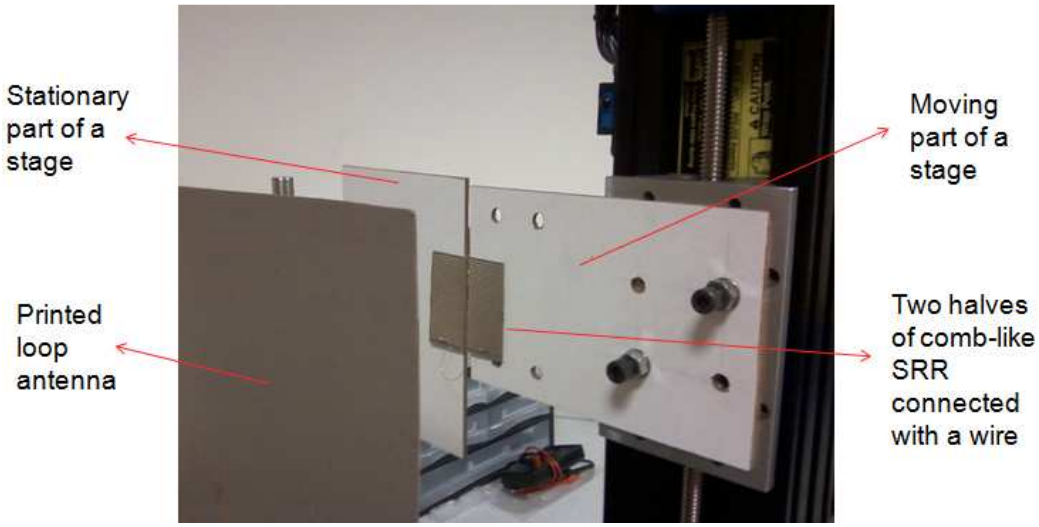

Figure 5.11 Full experimental setup.

Controlled motion of the moving part of the sensor has been provided by xyz-stage. With the help of xyz-stage, as one part of the comb-like SRR structure moves away from the stationary part, the gap between the teeth of the comb increases. At the beginning, the comb-like SRR part has moved away from the stationary part in 5 μm step size and as the gap width of the comb between teeth has increased, a frequency shift in the S_{11} response of the printed loop antenna is observed. S_{11} characteristics for different displacements have demonstrated that there is a monotonous relation between the gap width and resonance frequency of the comb-like SRR sensor as shown in Figure 5.13.

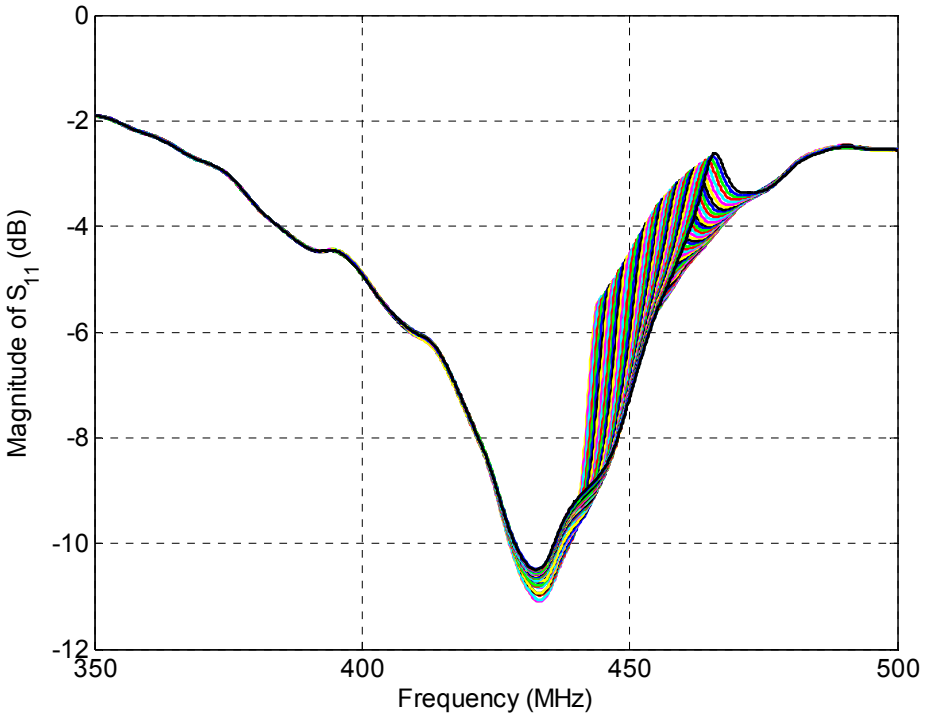

Figure 5.12 Magnitude of S_{11} vs. frequency graph for different displacement levels.

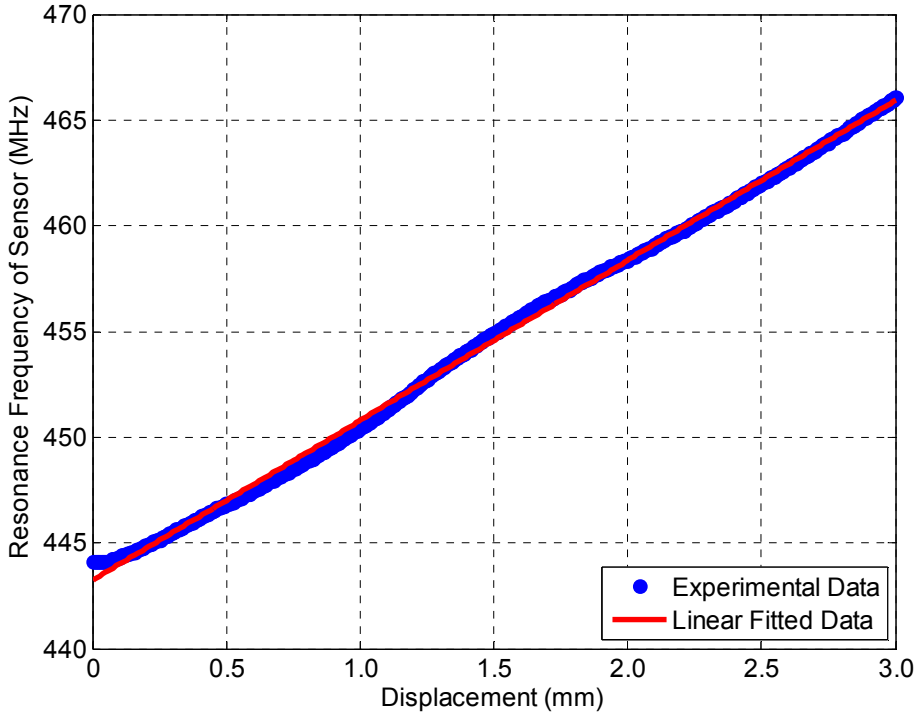

Figure 5.13 Resonance frequency of the comb-like SRR vs. displacement.

The linearity of the resonance frequency versus displacement has been investigated by computing the R-square value of the linear fitted data points. In this experiment, R-square value of the fitted experimental data has been found as 0.9985. Since this R-square value is greater than the predetermined minimum value of 0.95, the resonance frequency versus displacement can be accepted as linear. Therefore, it is concluded that as the gap width between the teeth pairs of the comb-like SRR increases in a controlled manner, the resulting resonance frequency of the comb sensor also increases linearly. This shows the convenience of the comb-like SRR structure for sensing applications.

After this observation, one of the comb parts has been moved away from the other stationary part in smaller step sizes and the relation between the displacement and resonance frequency of the comb has been once again examined. The smallest step size for a linear relationship between the displacement and the resonance frequency of the comb-like SRR has been experimentally found to be 1 μm. Therefore, if one part of the comb is displaced away from the other with an at least 1 μm step, the resonance frequency of the comb sensor increases proportionally as shown in Figure 5.15.

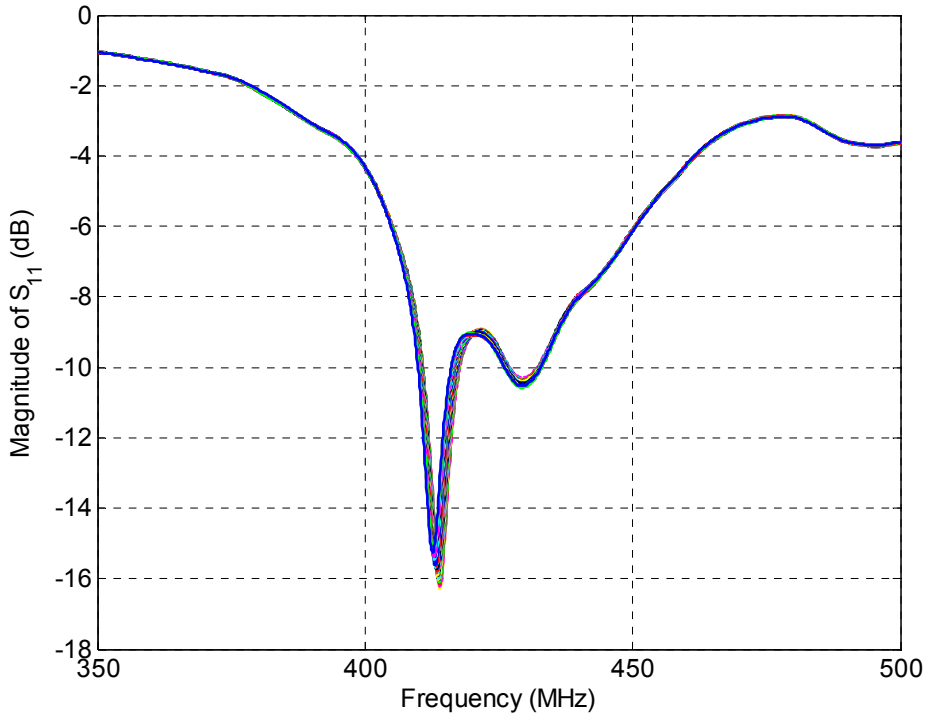

Figure 5.14 Magnitude of S_{11} vs. frequency for different displacement levels.

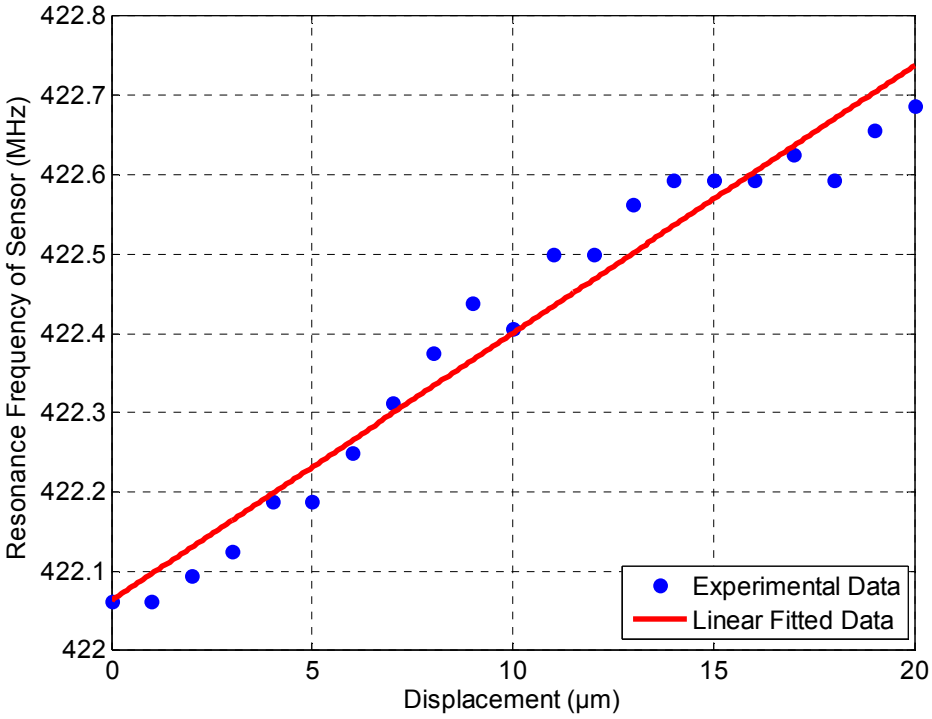

Figure 5.15 Resonance frequency vs. displacement of the comb-like SRR.

If we investigate the linearity of the resonance frequency versus displacement in Figure 5.15, we find that R-square value of the linear fitted data is equal to 0.9592. Again, since this value is greater than 0.95, original data points can be accepted as linear with a very small amount of error. Therefore, using this data for sensing applications is suitable.

During these experiments, we have observed that our sensor is sensitive to 1 μm change in the gap width between the teeth of comb-like SRR structure. Therefore, at least 1 μm change in the displacement can be monitored with the help of our comb-like SRR sensors. In addition, the maximum gap width for the dynamic range of our sensors has been found to 3 mm. This means that the displacement up to 3 mm can be observed using our sensors. As a result, our sensor has a resolution of 1 μm in the dynamic range of 3 mm.

5.6 Scaled-Down Loading Experiments

The experimental apparatus for mechanical loading in a scaled-down version of a building has been used for this second type of the experiments as shown in Figure 5.16.

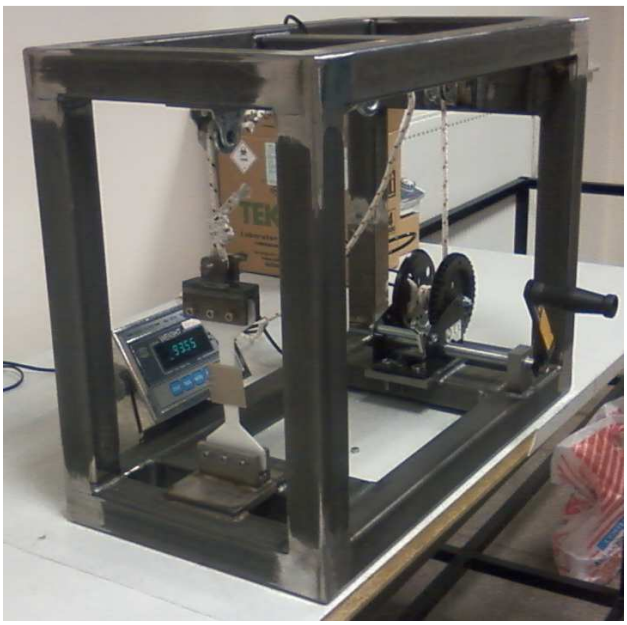

Figure 5.16 Scaled-down loading mechanism.

Since the Young modulus of the steel rods is nearly 200 GPa, which is a very high value, another material with lower Young modulus has been utilized to ease our experiments at lab. By considering the load level and corresponding elongation amount of the system with the application of the load, Delrin with a nearly 3.2 GPa Young modulus has been selected as our deformable platform. Therefore, our comb-like SRR sensor has been fixed to the Delrin platform.

With the help of this new experimental setup, as the tension is applied to the Delrin platform, strain is induced, which causes visible elongation in the Delrin platform. As a result of this elongation, change occurs in both the shape and frequency response of the fixed comb-like SRR sensor.

To begin our experiment, two parts of the comb sensor have been separately fixed to Delrin as shown in Figure 5.17.

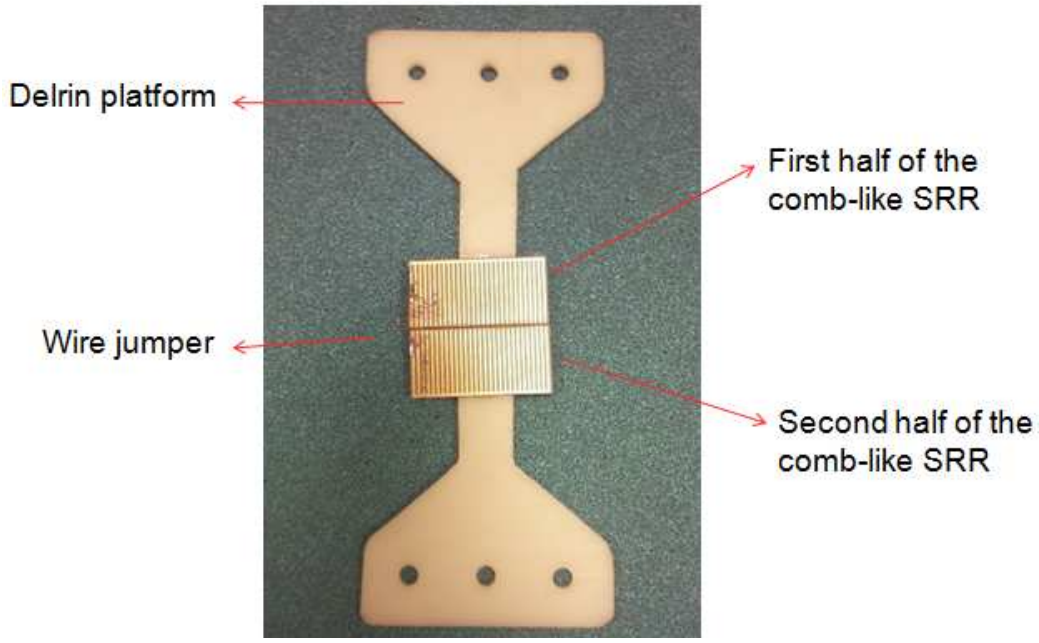

Figure 5.17 Our comb-like SRR sensor attached on the Delrin deformable platform.

This Delrin platform has been inserted into the new experimental setup, which is a scaled-down version of loading in buildings. A printed loop antenna connected to a calibrated network analyzer has been used at 15 cm away from the comb sensor as shown in Figure 5.18.

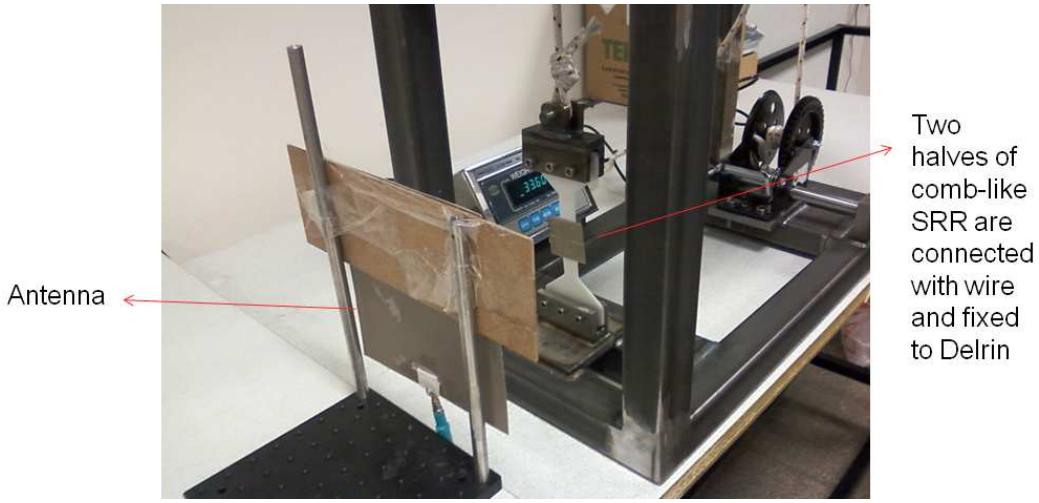

Figure 5.18 Full experimental setup.

The experiment has been started with the application of tension to the Delrin platform. Applied tension has led to elongation in the Delrin platform. As a result of this elongation, two parts of the comb sensor have separated from each other. Thus, the gap width between the teeth of the comb has increased with the applied tension to Delrin. As the displacement of the comb parts has increased, the frequency response of the sensor has shifted. A resonance frequency shift in the S_{11} response of the comb-like SRR sensor has been observed as a result of the displacement as shown in Figure 5.19.

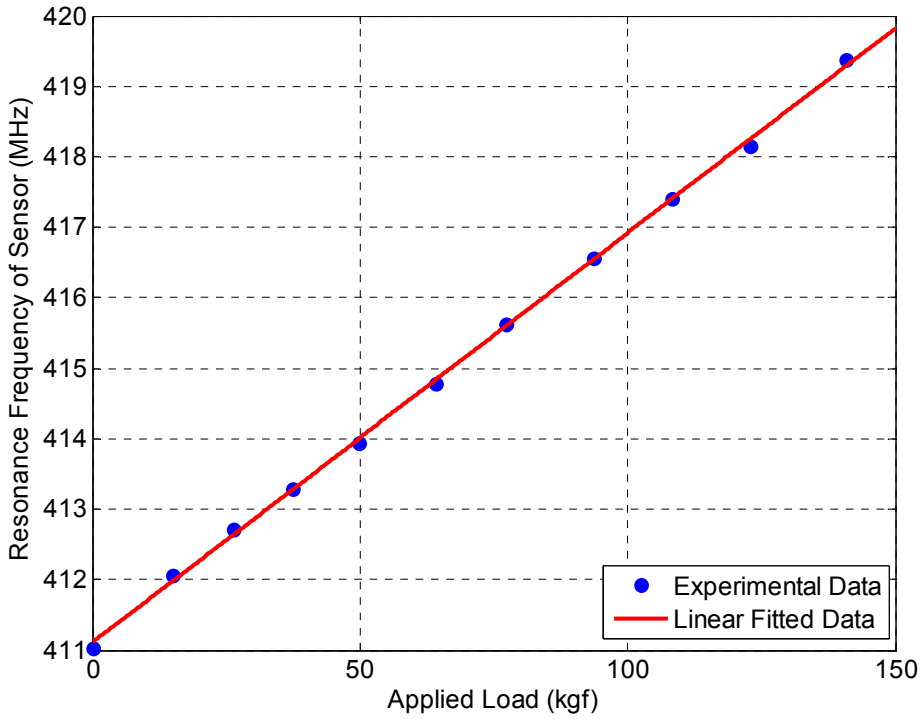

Figure 5.19 Resonance frequency vs. applied load.

To determine the linearity of the resonance frequency versus applied load, a linear fit has been applied to the original data points and R-square value of the linear fit has been calculated. For these experiment results in Figure 5.19, the R-square value has been found to be 0.9994. Since this R-square value is greater than 0.95 and also very close to 1, the original data on the resonance frequency versus applied load is considered nearly linear. As a result, by observing the

experimental results, it can be concluded that there is a linear relation between the applied load level and resonance frequency of the comb-like SRR structure. In other words, the resonance frequency of the comb-like SRR sensor increases linearly with the amount of tension applied to Delrin.

5.7 Loading Experiments Using Steel Rods

After observing the successful results of the previous experiments, we have performed the experiments with steel rods in collaboration with Dr. Özgür Kurç. For the application of tension to steel rods, we have used the experimental setup at Middle East Technical University Civil Engineering Department Laboratory. Experimental setup of this high-level loading mechanism is shown in Figure 5.20.

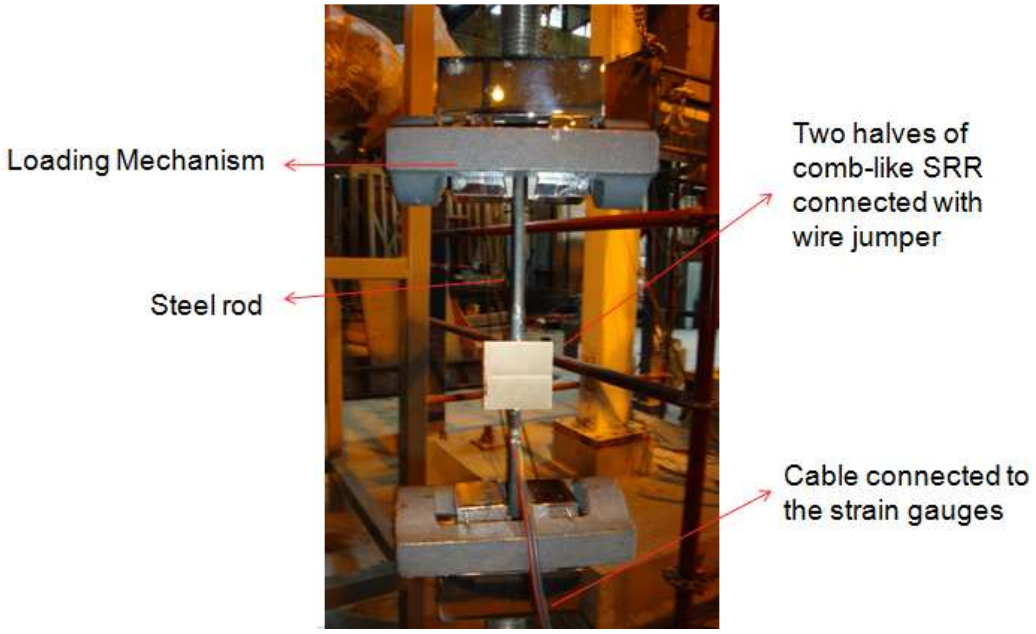

Figure 5.20 Loading mechanism at METU.

To start the experiment, two parts of the comb sensor have been fixed to steel rod with a diameter of 9 mm as shown in Figure 5.21.

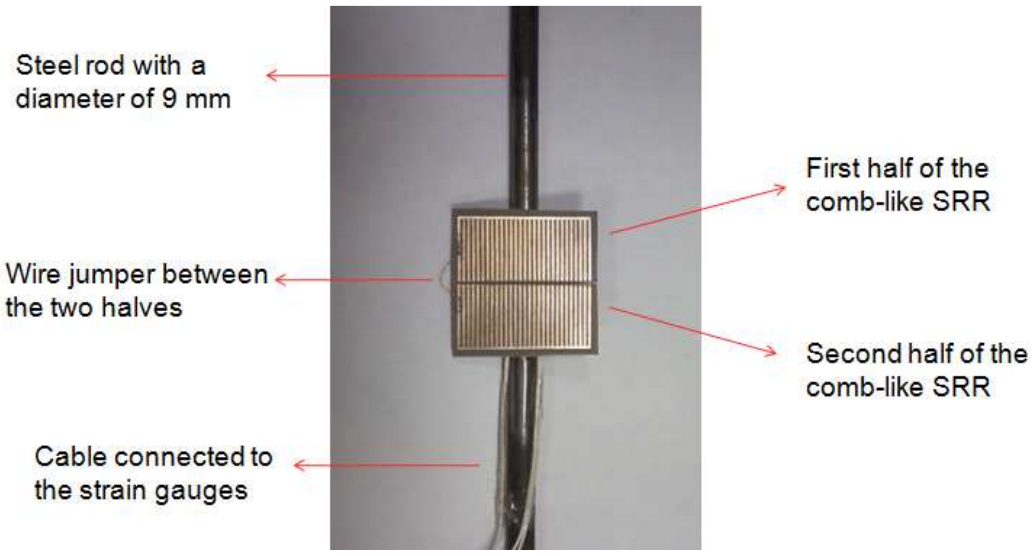

Figure 5.21 Comb-like SRR sensor attached on the steel rod.

To measure the amount of strain induced on the steel rod, three strain gages have been used. These strain gages have been fixed on three sides of the steel rod carefully as shown in Figure 5.22. As a result, three sides of the steel rod have been covered with the strain gages and the other side has our comb-like SRR sensor.

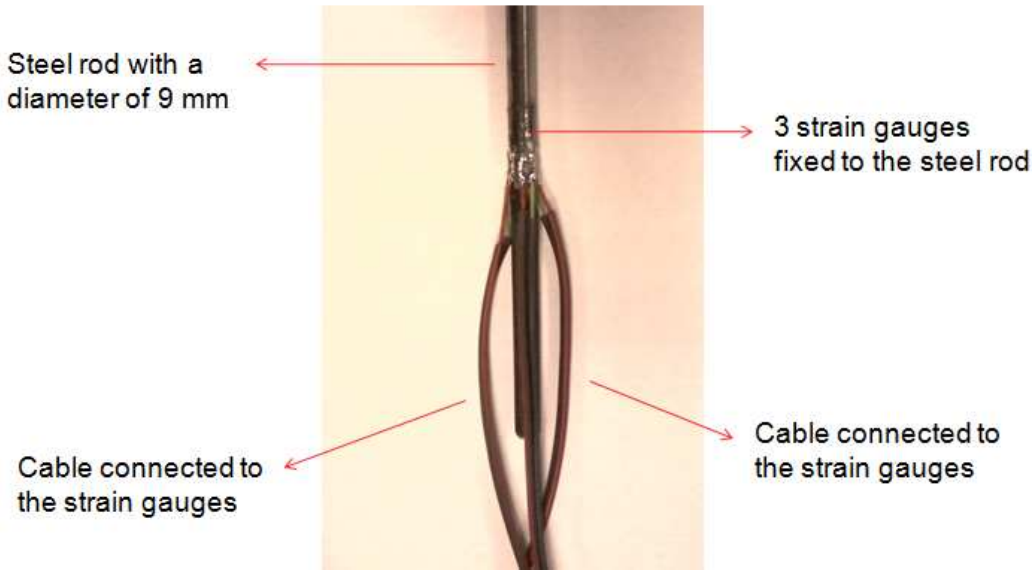

Figure 5.22 Strain gages on the steel rod.

For the elongation of the steel rod, a device called extensometer shown in Figure 5.23 has been used in our experiments. Extensometer has been attached to the steel rod such that our comb-like SRR sensor has been placed between the legs of the extensometer.

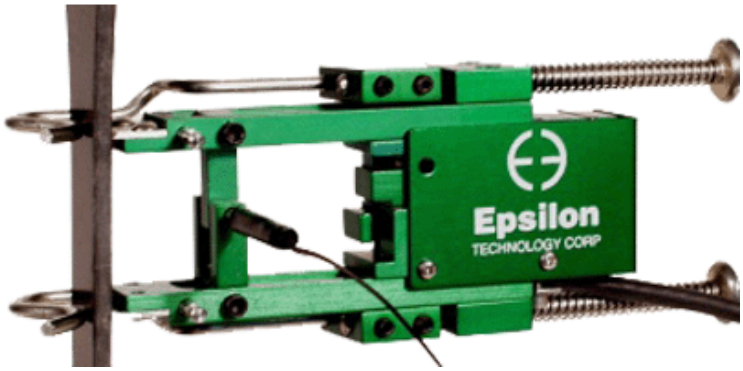

Figure 5.23 Extensometer.

Following these steps, a printed square shaped loop antenna, which is connected to a calibrated network analyzer, has been placed at 15 cm away from the comb-like SRR sensor and the experiment setup in Figure 5.24 has been constructed.

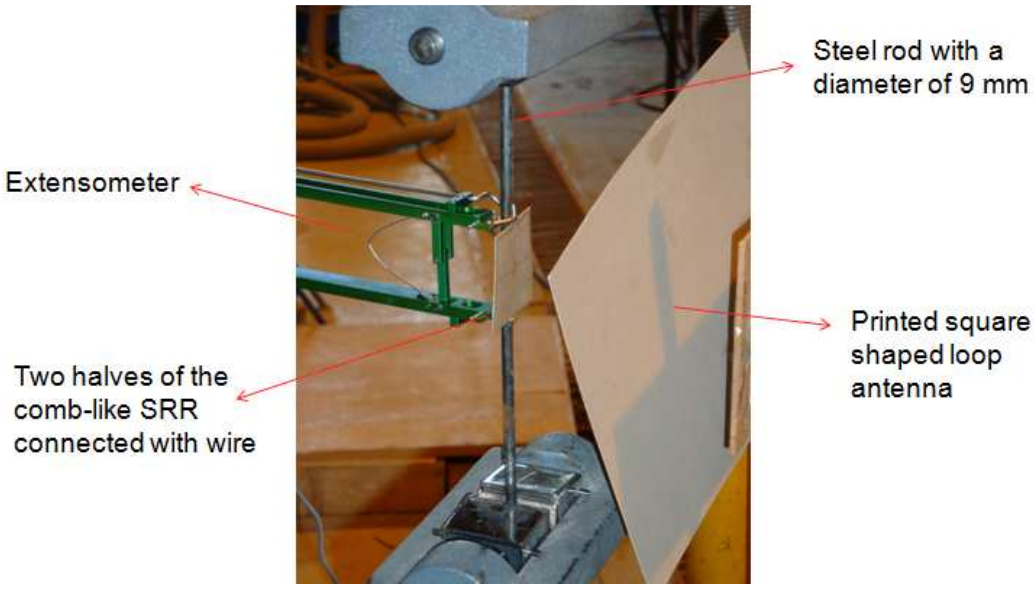

Figure 5.24 Full experimental setup.

Then, a piece of concrete with a thickness of 8 cm has been inserted between the antenna and the comb-like SRR sensor into the experimental setup as shown in Figure 5.25.

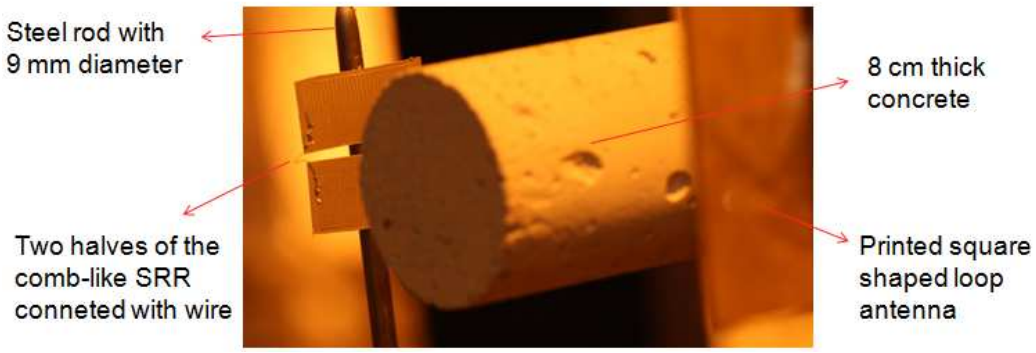

Figure 5.25 Full experimental setup with a concrete.

The experiment has begun with the application of tension to the steel rod with the help of the loading mechanism. The experiment data has been taken at each second up to the breaking of the steel rod. As a result of the applied tension, steel rod has elongated such that two parts of the comb sensor have separated from each other. Thus, the amount of gap width between the teeth of the comb has increased with the applied tension to steel rod. Since the displacement has increased, the frequency response of the sensor has changed. A resonance frequency shift in the S_{11} response of the comb sensor has been observed as a result of the displacement.

To observe all changes taking place overtime during the experiment, stress and elongation of the steel rod as well as strain on the sensor should be obtained. Elongation amount of the steel rod between the legs of the extensometer has been recorded as displacement. Stress has been calculated from the applied load by using (1). In addition, strain on the sensor has been obtained from the data taken with the strain gauges. The following measurements have been obtained from the experiment.

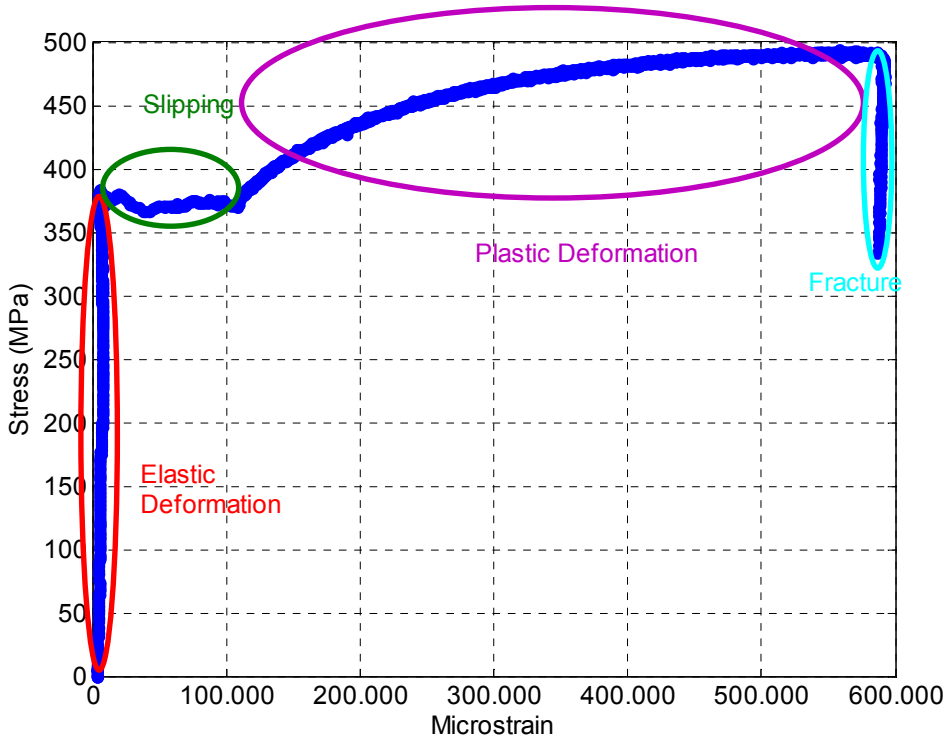

Figure 5.26 Stress vs. strain.

The steel rod experiences both the elastic and plastic deformations as it can be observed from Figure 5.26. The first region is the elastic deformation region where the relationship between stress and strain is linear. Deformation in the elastic region is recoverable. After the elastic region, slipping occurs and the cross sectional area of the steel rod decreases. Then, plastic deformation starts. In plastic deformation region, there occurs a nonlinear relationship between stress and strain. Irreversible effects occur in the steel rod in the slipping and plastic deformation regions. As a result of the increased stress, fracture happens at the end. Deformation regions can also be observed from Figure 5.27 where the displacement and stress data are present. Both the displacement and stress increase linearly in the elastic deformation region. When the slipping starts, a nonlinear increse occurs in the stress level. After the slipping region, plastic deformation occurs.

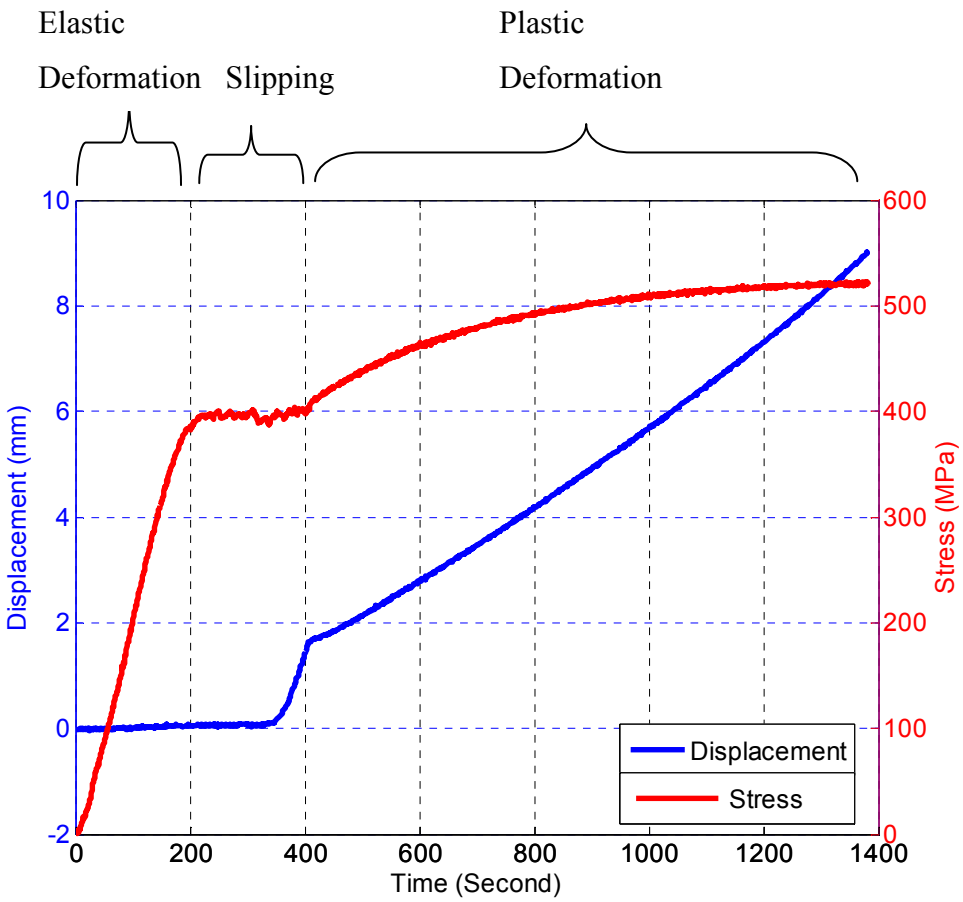

Figure 5.27 Displacement and stress vs. time.

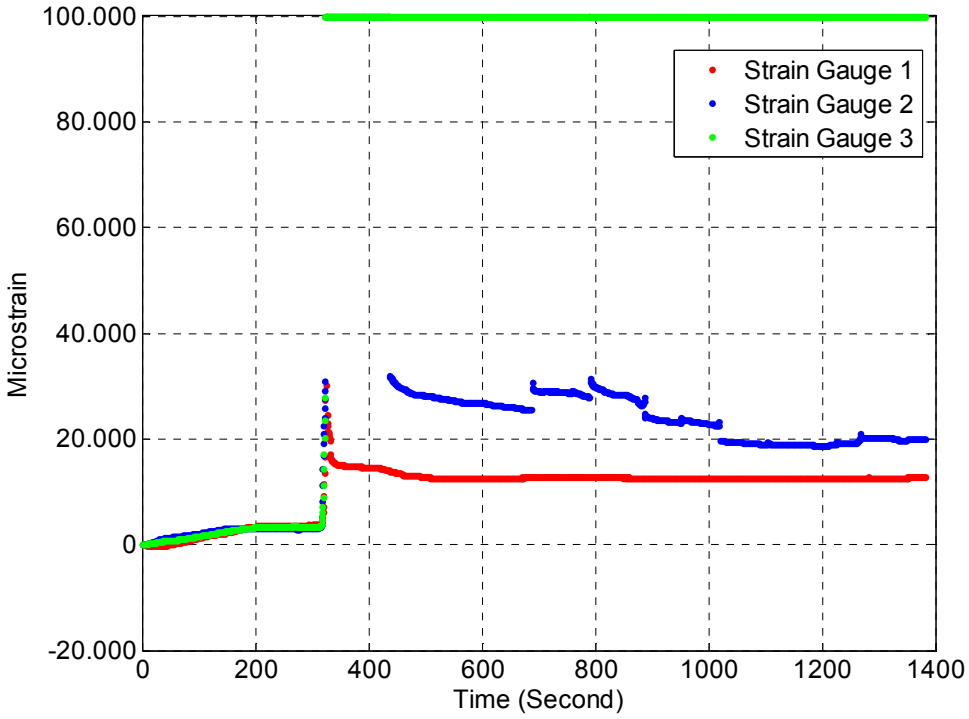

Figure 5.28 Strain vs. time.

As it can be seen from Figure 5.28, nearly 300 seconds after the start, the attachment between the strain gauges and steel rod becomes improper, which is common for these strain gauges and the apoxy used. Therefore, data taken with strain gages cannot be used to obtain strain on the sensor after 300 seconds. However, strain after 300 seconds can be calculated from the amount of elongation by using (2).

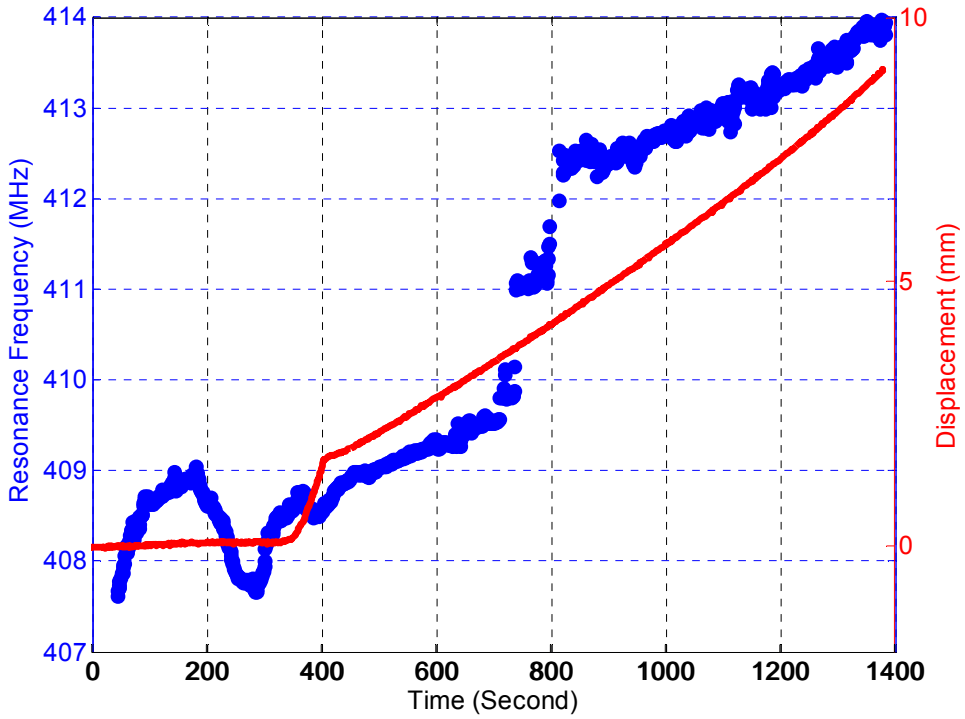

Figure 5.29 Resonance frequency and displacement vs. time.

It is clear from Figure 5.29 that the resonance frequency and displacement behaviours are very similar with respect to time. However, there occurs a jump in the behaviour of the resonance frequency nearly 800 seconds after the start. This is due to the unwanted orientation change of the sensor as it has been observed in the video recording of the experiment. This jump in resonance frequency also appears in Figures 5.30, 5.31, and 5.32, as expected.

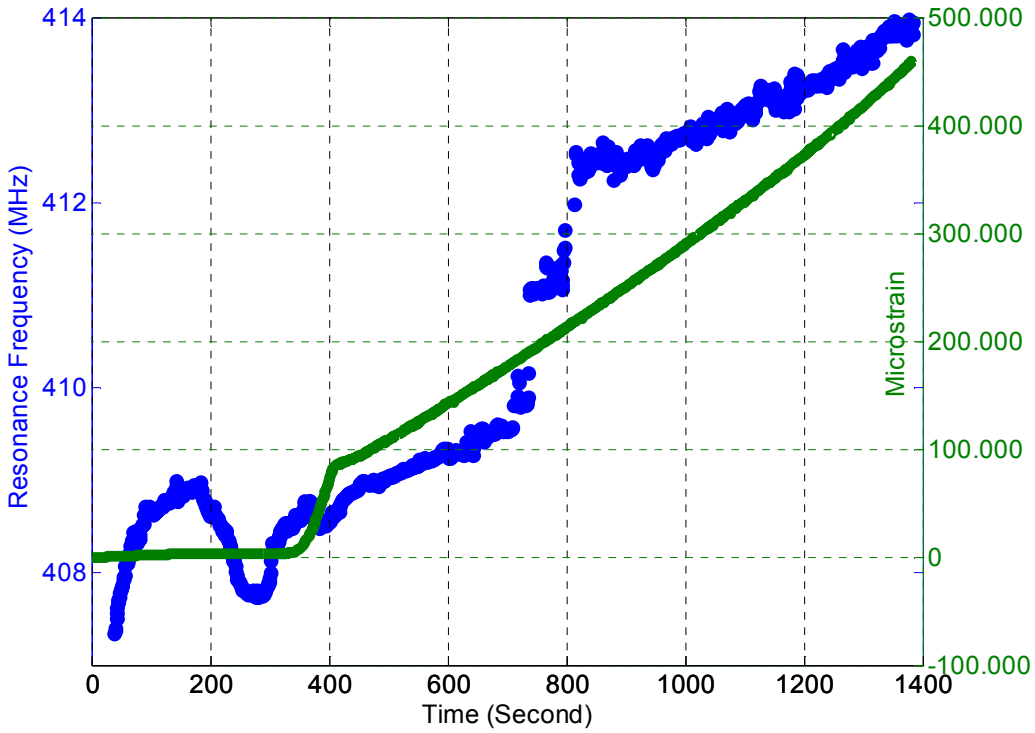

Figure 5.30 Resonance frequency and strain vs. time.

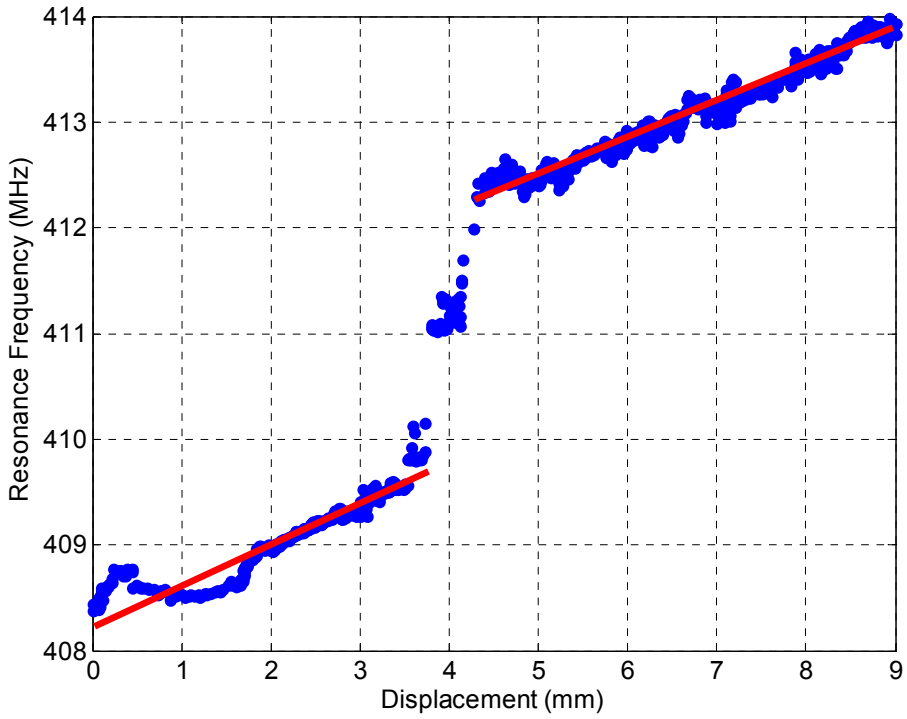

Figure 5.31 Resonance frequency vs. displacement.

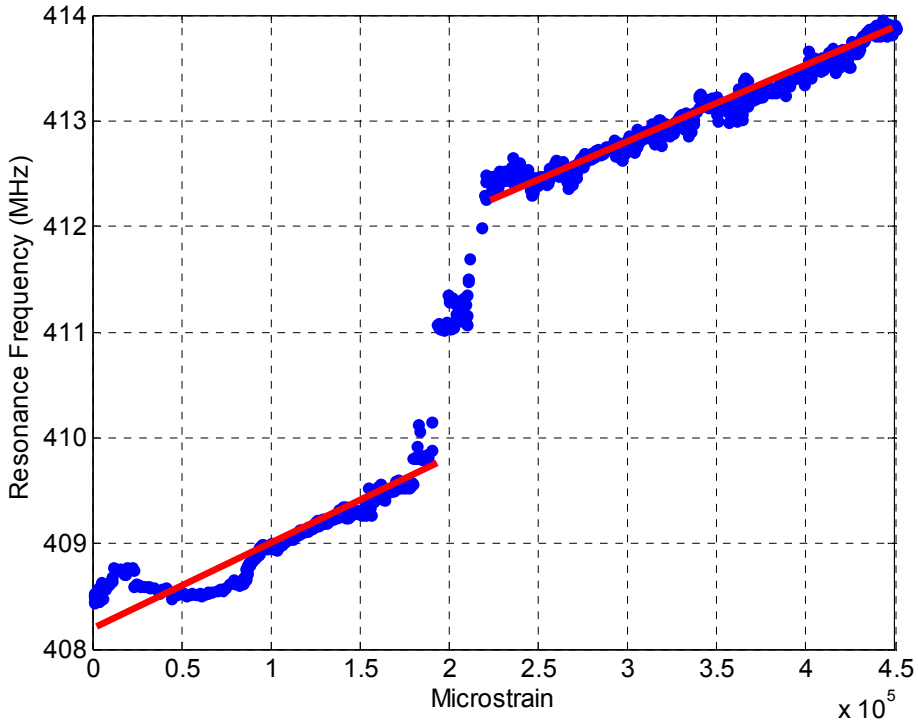

Figure 5.32 Resonance frequency vs. strain.

Figure 5.30 also exhibits the same similar behaviour of the resonance frequency with respect to strain level in time. As explained previously, a little change in the orientation of the sensor causes a jump in the resonance frequency nearly 800 seconds after the start. Figures 5.31 and 5.32 are further proofs of the monotonous relationship between the resonance frequency and the displacement and also between the resonance frequency and the strain level except for the mechanical noise. Piecewise linear relationships have been obtained due to the orientation change of the comb-like SRR sensor as explained previously.

The linearity of the resonance frequency versus displacement in Figure 5.31 has been investigated by computing the R-square value of the piecewise linear fitted data points. Linear fitting (shown with red line in Figure 5.31) has been applied to the experimental data separately before and after the jump in the resonance frequency. R-square value of the fitted experimental data has been found as 0.9503 before the jump. Moreover, R-square value is equal to 0.9635

after the jump in the resonance frequency. Since these R-square values are greater than the predetermined minimum value of 0.95, the resonance frequency versus displacement can be accepted as linear.

If we investigate the piecewise linearity of the resonance frequency versus strain in Figure 5.32, we find two R-square values before and after the jump in the resonance frequency. R-square value of the linear fitted data (shown with red line in Figure 5.32) is equal to 0.9517 before the jump whereas it equals to 0.9624 after the jump in the resonance frequency. Again, since these values are greater than 0.95, original data points can be accepted as linear with a very small amount of error.

As a result, from Figures 5.29, 5.30, 5.31 and 5.32, it can be said that the resonance frequency of the comb-like SRR sensor increases as a general trend with the increase in the displacement and strain amounts, if we ignore the noise coming from mechanical instability.

In the real experiment, the steel rod experiences elastic and plastic regions of the deformation as it can be observed from the stress versus strain curve in Figure 5.26. Moreover, by using the knowledge in Figure 5.28 for strain gauges, it can be concluded that our comb-like SRR sensor can be used to observe the health of a structure built using steel rods also in the plastic deformation when the classical strain gauges are not useful. Therefore, our comb-like SRR sensor can be used for sensing applications successfully to observe strain and elongation amounts both in elastic and plastic deformation regions.

Chapter 6

Conclusions

Measuring the strain level of a structure is a very important issue for the civil engineering. Despite some challenges in real time strain monitoring, this issue is crucial to determine the health of a structure especially before and after the earthquakes. To cater this need and observe a strain level for real time structural health monitoring, we have designed metamaterial-based, passive, wireless, radio frequency strain sensors in the form of comb-like split ring resonators. In this work, our aim is to provide a quantitative data for structural health monitoring by observing a strain level of the buildings in real time.

Architecture of proposed sensors is based on a multiple split ring resonator design. These sensors rely on a simple principle of operation. They are easy to fabricate and cost effective. They are composed of nested split ring resonators in the form of comb-like structures and require external antennas for read-out. In operation, such an antenna is preferred to have a narrow band, and the resonant frequency of the sensor is expected to be close to the operating frequency of the antenna. For that purpose, we also designed and implemented printed loop antennas to match our sensors.

Due to the resonator behaviour, split ring resonator based sensors have a predetermined resonance frequency. When the load is applied to the structure on which the sensor is mounted, the resulting strain causes deformation and change in the displacement of the sensor parts. With these changes in the sensor, a resonance frequency shift occurs in the sensor response. Several experiments that use a single comb-like SRR sensor have been performed. In all experiments, it has been observed that the frequency shift in S_{11} is found to be monotonously

increasing with the change in the displacement, an amount of applied load and strain level of the structure.

Although the parts of a structure on which the proposed sensors are intended to be mounted are made of steel rods, the first displacement experimental setup for a proof-of-concept study is designed for controlled precise positioning of parts of the comb sensors. These experimental results show that there is a linear relation between the gap width and the resonance frequency of the comb-like SRR sensor. For the second set of experiments, the experimental apparatus for mechanical loading in a scaled-down version of a building is used. In these experiments, the load is applied to the structure and the effects of the load on the resonance frequency shift of the comb-like SRR sensor are investigated. It is clear from the experimental results that the resonance frequency of the comb sensor has a linear relationship with the applied load amount. After the success of these two experiment sets, a real experimental setup with a piece of concrete inserted between the sensor and the antenna is used for the application of the load to the steel rods, which are used for the buildings. It can be understood from these experimental results that the resonance frequency of the comb-like SRR sensor changes accordingly with the elongation and strain amount of the rod. It can be concluded that our comb-like SRR sensor can be used for sensing applications in the concrete environment effectively to obtain strain and elongation amounts both in elastic and plastic deformation regions even if the classical strain gauges are not useful.

To summarize, we developed passive, wireless, RF sensors based on SRR architectures. Our experimental results indicate correlated frequency shift of the sensor resonance with the displacement, load and strain variation. These sensors are very useful also in the plastic deformation of the steel rods when the classical strain gauges cannot be used. By monitoring the displacement on the steel rods telemetrically, these SRR sensors hold promise for real-time SHM.

In our experimental work, we have observed that our sensor is sensitive to 1 μm change in the gap width and it can be used up to 3 mm displacement. This means that our sensor has a sensitivity of 1 μm and a dynamic range of 3 mm. As a next step, our comb-like SRR sensor can be optimized for different strain monitoring operations by improving the sensitivity and dynamic range. In addition, we have conducted all presented simulations and experiments at a fixed distance (15 cm) between the antenna and sensor since the output power of the network analyzer is limited. To increase the distance between the antenna and sensor, the signal power should be increased. Therefore, by increasing the power level and the distance between the sensor and antenna, remote sensing can be demonstrated in the future work. Another future work may include combining different sensors operating at different frequencies to monitor strain simultaneously at different spots or in different directions.

Bibliography

[1] J. Wu, S. Yuan, S. Ji, G. Zhou, Y. Wang, and Z. Wang, "Multi-agent system design and evaluation for collaborative wireless sensor network in large structure health monitoring," *Expert Systems with Applications*, vol. 37, p. 2028, 2010.

[2] N. A. Tanner, J. R. Wait, C. R. Farrar, and H. Sohn, "Structural health monitoring using modular wireless sensors," *Journal of Intelligent Material Systems and Structures*, vol. 14, p. 43, 2003.

[3] B. F. Spencer Jr, M. E. Ruiz-Sandoval, and N. Kurata, "Smart sensing technology: opportunities and challenges," *Journal of Structural Control and Health Monitoring*, vol. 11, p. 349, 2004.

[4] Ali Daliri, Amir Galehdar, Sabu John, Wayne Rowe, and Kamran Ghorbani, "Circular Microstrip Patch Antenna Strain Sensor for Wireless Structural Health Monitoring," *Proceedings of the World Congress on Engineering*, vol. 2, p. 1173, 2010.

[5] T. Nagayama, M. Ruiz-Sandoval, B. F. Spencer Jr., K. A. Mechitov, and G. Agha, "Wireless Strain Sensor Development for Civil Infrastructure," *Proceedings of First International Workshop on Networked Sensing Systems*, vol. 5, p. 97, 2004.

[6] I. Kang, M. J. Schulz, J. H. Kim, V. Shanov, and D. Shi, " A carbon nanotube strain sensor for structural health monitoring," *Smart Materials and Structures*, vol. 15, p. 737, 2006.

[7] R. O. Claus, M. F. Gunther, A. Wang, and K. A. Murphy, "Extrinsic Fabry-Perot sensor for strain and crack opening displacement measurement from −200 to 900 °C," *Smart Materials and Structures*, vol. 1, p. 237, 1992.

[8] C.I. Merzbacher, A.D. Kersey, and E.J. Friebele, "Fibre-optic sensors in concrete: A review," *Smart Materials and Structures*, vol. 5, p. 196, 1996.

[9] R. Melik, E.Unal, N. Kosku Perkgoz, B. Santoni, D. Kamstock, C. Puttlitz, and H. V. Demir, "Nested Metamaterials for Wireless Strain Sensing," *IEEE Journal of Special Topics in Quantum Electronics* (special issue on Metamaterials), vol. 16, p. 450, 2010.

[10] D. F. Sievenpiper, M. E. Sickmiller, and E. Yablonovitch, "3d wire mesh photonic crystals," *Physical Review Letters*, vol. 76, p. 2480, 1996.

[11] J. B. Pendry, A. J. Holden, W. J. Stewart, and I. Youngs, "Extremely Low Frequency Plasmons in Metallic Mesostructures," *Physical Review Letters*, vol. 76, p. 4773, 1996.

[12] S. I. Maslovski, S.A. Tretyakov, and P.A. Belov, "Wire media with negative effective permittivity: A quasi-static model," *Microwave* and Optical *Technology* Letters, vol. 35, p. 47, 2002.

[13] V. G. Veselago, "The electrodynamics of substances with simultaneously negative values of permittivity and permeability," *Soviet Physics Uspekhi*, vol. 10, p. 509, 1968.

[14] J. B. Pendry, A. J. Holden, D. J. Robbins, and W. J. Stewart, "Low frequency plasmons in thin-wire structures," *Journal of Physics: Condensed Matter*, vol. 10, p. 4785, 1998.

[15] D. R. Smith, D. C. Vier, Willie Padilla, Syrus C. Nemat-Nasser, and S. Schultz, "Loop-wire medium for investigating plasmons at microwave frequencies," *Applied Physics Letters*, vol. 75, p. 1425, 1999.

[16] J.B. Pendry, A.J. Holden, D.J. Robbins, and W.J. Stewart, "Magnetism from Conductors and Enhanced Nonlinear Phenomena," *IEEE Transactions on Microwave Theory and Techniques*, vol. 47, p. 2075, 1999.

[17] D. R. Smith, Willie J. Padilla, D. C. Vier, S. C. Nemat-Nasser, and S. Schultz, "Composite medium with simultaneously negative permeability and permittivity," *Physical Review Letters,* vol. 84, p. 4184, 2000.

[18] R. A. Shelby, D. R. Smith, S. C. Nemat-Nasser, and S. Schultz, "Microwave transmission through a two-dimensional, isotropic, lefthanded metamaterial," *Applied Physics Letters*, vol. 78, p. 489, 2001.

[19] D. Schurig, J. J. Mock, B. J. Justice, S. A. Cummer, J. B. Pendry, A. F. Starr, and D. R. Smith, "Metamaterial electromagnetic cloak at microwave frequencies," *Science*, vol. 314, p. 977, 2006.

[20] J. B. Pendry, "Negative refraction makes a perfect lens," *Physical Review Letters*, vol. 85, p. 3966, 2000.

[21] M. C. K. Wiltshire, J. B. Pendry, I. R. Young, D. J. Larkman, D. J. Gilderdale, and J. V. Hajnal, "Microstructured magnetic materials for rf flux guides in magnetic resonance imaging," *Science*, vol. 291, p. 849, 2001.

[22] R. Marqu´es, F. Mesa, J. Martel, and F. Medina, "Comparative Analysis of Edge- and Broadside-Coupled Split-ring Resonators for Metamaterial Design - Theory and Experiments," *IEEE Transactions on Antennas and Propagation*, vol. 51, p. 2572, 2003.

[23] B. Sauviac, C.R. Simovski, and S.A. Tretyakov, "Double split-ring resonators: Analytical modeling and numerical simulations," *Electromagnetics*, vol. 24, p. 317, 2004.

[24] F. Falcone, T. Lopetegi, J.D. Baena, R. Marqu´es, F. Mart´ın, and M. Sorolla, "Effective Negative-Stopband Microstrip Lines Based on Complementary Split-Ring Resonators," *IEEE Microwave Theory and Wireless Component Letters*, vol. 14, p. 280, 2004.

[25] S.N. Burokur, M. Latrach, and S. Toutain, "Study of the Effect of Dielectric Split-Ring Resonators on Microstrip-Line Transmission," *Microwave and Optical Technology Letters*, vol. 44, p. 445, 2005.

[26] T. Koschny, M. Kafesaki, E. N. Economou, and C. M. Soukoulis, "Effective Medium Theory of Left-Handed Materials," *Physical Review Letters*, vol. 93, p. 107402, 2004.

[27] R. Marques, F. Medina, and R. Rafii-El-Idrissi, "Role of bianisotropy in negative permeability and left-handed metamaterials," *Physical Review B*, vol. 65, p. 144440, 2002.

[28] C.A. Balanis, "Antenna Theory: Analysis and Design," John Wiley & Sons., 2005

[29] "The ARRL Handbook for Radio Communications," The American Radio Relay League, 2010

[30] D. M. Pozar, "Microwave Engineering," John Wiley & Sons., 2005